

IEA Wind Task 46
Erosion of wind turbine blades

**Atmospheric drivers of wind
turbine blade leading edge
erosion: Hydrometeors**

Technical report



iea wind

Technical Report

Atmospheric drivers of wind turbine blade leading edge erosion: Hydrometeors

Prepared for the
International Energy Agency Wind Implementing Agreement

Prepared by
IEA Task 46, Workpackage #2

Lead author:

Sara C. Pryor (Cornell University)*

* correspondence to; sp2279@cornell.edu

Co-authors:

Rebecca J. Barthelmie (Cornell University)

Jeremy Cadence (WEICan)

Kirsten Dyer (ORE Catapult)

Charlotte Hasager (DTU)

Robbie Herring (ORE Catapult)

Stephan T. Kral (University of Bergen)

Raul Prieto (VTT)

Joachim Reuder (University of Bergen)

Marianne Rodgers (WEICan)

Marijn Veraat (Ørsted)

Date: 5 November 2021

IEA Wind TCP functions within a framework created by the International Energy Agency (IEA). Views, findings, and publications of IEA Wind do not necessarily represent the views or policies of the IEA Secretariat or of all its individual member countries. IEA Wind is part of IEA's Technology Collaboration Programme (TCP).

Purpose

Leading edge erosion (LEE) of wind turbine blades has been identified as a major factor in decreased wind turbine blade lifetimes and energy output over time. Accordingly, the International Energy Agency Wind Technology Collaboration Programme (IEA Wind TCP) created Task 46 to undertake cooperative research in the key topic of blade erosion. Participants in this task are given in Table 1.

The Task 46 under IEA Wind TCP is designed to improve understanding of the drivers of LEE, the geospatial and temporal variability in erosive events; the impact of LEE on the performance of wind plants and the cost/benefit of proposed mitigation strategies. Furthermore Task 46 seeks to increase the knowledge about erosion mechanics and the material properties at different scales, which drive the observable erosion resistance. Finally, the Task aims to identify the laboratory test setups which reproduce faithfully the failure modes observed in the field in the different protective solutions.

This report is a product of WorkPackage 2 **Climatic conditions driving blade erosion**. The objectives of the work summarized in this report are to:

- Describe crucial meteorological parameters for wind turbine blade leading edge erosion
- Describe technologies appropriate to measurement of hydroclimates and specifically hydrometeor size distributions and phase
- Identify data sets that are available to describe hydrometeor size distributions and phase and generate meta-data for data sets available for use in mapping wind turbine blade leading edge erosion potential. Accompanying this report is a detailed spreadsheet that summarizes those meta-data. That file is entitled: IEA46_WP2_METADATA_Deliverable1_5November2021.xlsx. The doi for this dataset is 10.5281/zenodo.5648211. Included in this report are summary analyses based on these key datasets.
- Identify priority geographic areas for geospatial mapping of wind turbine blade leading edge erosion potential

This report is released for public dissemination.

Table 1 IEA Wind Task 46 Participants during period 2021-2025*

Country	Contracting Party	Active Organizations
Belgium	The Federal Public Service of Economy, SMEs, Self-Employed and Energy	Engie
Canada	Natural Resources Canada	WEICan
Denmark	Danish Energy Agency	DTU (co-OA), Hempel, Ørsted A/S
Finland	Business Finland	VTT (co-OA)
Germany	Federal Ministry for Economic Affairs and Climate Action	Fraunhofer IWES, Covestro, Emil Frei (Freilacke), Nordex Energy SE
Ireland	Sustainable Energy Authority of Ireland	IT Carlow, NUI Galway, University of Limerick
the Netherlands	Netherlands Enterprise Agency	TU Delft, Suzlon, TNO
Norway	Norwegian Water Resources and Energy Directorate	Equinor Energy AS, University of Bergen
Spain	CIEMAT	CENER, Aerox Advanced Polymers, CEU Cardenal Herrera University, Siemens Gamesa Renewable Energy, Nordex Energy Spain
United Kingdom	Offshore Renewable Energy Catapult	ORE Catapult, University of Bristol
United States	U. S. Department of Energy	Cornell University, Sandia National Laboratories, 3M

*Participants are listed as of November 2021

Table of Contents

Purpose	3
1 Content and structure of this report.....	11
2 Identification of crucial meteorological parameters for wind turbine blade leading edge erosion.....	11
2.1 Closing velocity	11
2.2 Size distributions of hydrometeors	13
2.3 Precipitation phase	15
2.4 Impingement efficiency of hydrometeors on the leading edge.....	15
3 Measurement approaches	16
3.1 Direct in situ measurement technologies	16
3.1.1 Tipping bucket rain gauges.....	16
3.1.2 Disdrometers.....	16
3.1.3 Hail sensors	18
3.2 Remote sensing technologies.....	18
3.2.1 RADAR	18
3.2.2 Dual-polarization RADAR	20
3.2.3 Micro-rain RADAR	21
3.2.4 Satellite-derived products	21
3.2.5 Gridded data sets	21
3.2.6 Numerical Weather Prediction models	22
4 Data availability for use in mapping wind turbine blade leading edge erosion potential	23
4.1 Hydrometeor size distribution measurements: Locations	23
4.1.1 Norway.....	23
4.1.2 Wind Energy Institution of Canada (WEICan)	24
4.1.3 U.S. Department of Energy Atmospheric Radiation Measurement (ARM) sites	24
4.1.4 UK onshore	25
4.1.5 Offshore waters of the UK	25
4.1.6 Denmark	25
4.1.7 Network operated by Orsted	25
4.2 Examples of measured droplet size distributions.....	25
4.3 Variability in rainfall rates and droplet size distributions as a function of instrument	32
4.4 Variability in droplet size distributions as a function of event and season	33
5 Identification of priority geographic areas for geospatial mapping of wind turbine blade leading edge erosion potential.....	35
6 Key Conclusions/Recommendations	37
7 References.....	38
8 Appendix A: Vocabularies/definitions.....	43
8.1 Relevant definitions from the World Meteorological Organization	43

- 8.2 Relevant definitions from the International Electrotechnical Commission43
- 8.3 Relevant definitions from the ontology hosted at DTU Wind Energy43
- 8.4 World Meteorological Organization (WMO) synoptic present weather codes (Table 4680):44
- 9 Appendix B: METADATA46

List of Figures

Figure 1 Terminal fall velocities for rain droplets and hail computed using Equations (1) and (2) and the following assumptions: $\rho_o = 1.225 \text{ kgm}^{-3}$, $\rho_{air} = 0.999 * \rho_o$, $\rho_i = 900 \text{ kgm}^{-3}$	12
Figure 2 Illustrative example of wind turbine RPM and tip speed as a function of wind speed for the IEA 15 MW reference turbine (Gaertner et al. 2020). Power production begins at 4 ms^{-1} and ceases at wind speeds $> 25 \text{ ms}^{-1}$, thus no RPM or tip-speed data are plotted for wind speeds outside of the range of $4\text{-}25 \text{ ms}^{-1}$	12
Figure 3 Illustrative example of the number size distribution of raindroplets for different rainfall rates (RR) as described using the Marshall-Palmer size distribution (Eq. 3). The left panel shows hydrometeor radii of $0\text{-}15 \text{ mm}$, while the panel on the right confines the radii to $0\text{-}3 \text{ mm}$	14
Figure 4 Illustrative example of the number size distribution of rain droplets for different rainfall rates (RR) as described using the Best size distribution (Eq. 4). The left panel shows hydrometeor radii of $0\text{-}15 \text{ mm}$, while the panel on the right confines the radii to $0\text{-}3 \text{ mm}$	14
Figure 5 Ratio of impact speed to upstream speed for particles impinging on a blade. .	15
Figure 6 Evaluation of NORA3 wind speeds. Upper panels show hourly mean wind speed at 50 m (left panel) and 100 m (right panel) from NORA3 and the New European Wind Atlas (NEWA) compared to cup anemometer measurements from the FINO1 platform in the North Sea for the year 2009. Lower panels show the mean wind speed at 100 m (left panel) and 500 m (right panel) from NORA3 compared to lidar wind profiles measured with a Leosphere WindCube 100S at the FINO 1 platform during the OBLEX-F1 campaign in 2015 and 2016.....	23
Figure 7 Mean droplet-size distribution measured by a micro-rain RADAR (MRR) between 100 m a.g.l. and 300 m a.g.l. in Bergen Norway during the year 2019.	26
Figure 11 Droplet-size distribution measured by a Campbell Scientific PWS100, at an elevation of 11 meters at the North Cape wind farm in Prince Edward Island, Canada from October 2018 through December 2020. Note: No instances of $\text{RR} > 17 \text{ mmhr}^{-1}$ are present in this dataset.	26
Figure 8 Mean droplet-size distribution measured by a ground-based Parsivel ² disdrometers at the Lamont Southern Great Plains DoE ARM site (left) and the Billings Southern Great Plains DoE ARM sit (right) during the year 2019. Note the axes are different in the two frames and have been scaled to optimally present the data range at each site. Droplet size distributions are only shown for RR classes with > 50 data samples, but RR classes are represented by any data samples are included in the legend.	28
Figure 9 Mean droplet-size distribution measured by an impact disdrometer (left) and a video disdrometer (right) at the Lamont Southern Great Plains DoE ARM site during the year 2019. Droplet size distributions are only shown for RR classes with > 50 data samples, but RR classes are represented by any data samples are included in the legend.	28
Figure 11 Mean droplet-size distribution measured by ground-based (Thies) disdrometers at the Cairngorm site in Scotland (upper left), Reading (upper right) and Weybourne (lower left) in England during the year 2018. Note the axes are different in the two frames	

and have been scaled to optimally present the data range at each site. Droplet size distributions are only shown for RR classes with > 50 data samples, but RR classes are represented by any data samples are included in the legend.29

Figure 12 Mean droplet-size distribution across a range of rain rates (mmhr^{-1}) measured by PWS100 Campbell Scientific disdrometers deployed offshore at (left) National Offshore Anemometry Hub off the Northeast coast of England and (right) Levenmouth Demonstration Turbine off the East coast of Scotland from August 2018 and December 2020, respectively, to present. Note periods with higher RR than those displayed have been observed at both sites.30

Figure 13 Mean droplet-size distribution measured by a ground-based Parsivel² disdrometers at the Horns Rev 3 wind farm during February 2019 to February 2020 (left) and during 2019 on the DTU campus at Risø (right). Note the axes are different in the two frames and have been scaled to optimally present the data range at each site. There appear to be no valid data at Horns Rev 3 for rainfall rates above approximately 16 mmhr^{-1}31

Figure 14 Mean droplet-size distribution measured by a ground-based Parsivel² disdrometer at the Horns Rev 2 wind farm off the west coast of Denmark during December 2018 to October 2021 Note there are very few valid data for rainfall rates above approximately 10 mmhr^{-1}31

Figure 15 Left: Scatterplots of 1-minute rainfall rates (mmhr^{-1}) from the four disdrometers (D1-D4). Right: Mean droplet size spectrum from those disdrometers. Data collected at Cornell University Ithaca, NY during 21-29 October 2021. 2600 1-minute periods exhibited non-zero RR.33

Figure 16 The 10th and 90th percentile values of the droplet number concentration in each size class based on measurements by a ground-based Parsivel² disdrometer at the DoE ARM observatory at Lamont in the U.S. Southern Great Plains during 2019.34

Figure 17 Mean droplet-size distribution measured by a ground-based Parsivel² disdrometer at the DoE ARM observatory at Lamont in the U.S. Southern Great Plains based on data from 2017-2019, inclusive (left). The cumulative probability distribution for $\text{RR} > 0.2 \text{ mmhr}^{-1}$ based on the same data set. For legibility the x-axis has been truncated to only show RR of $1\text{-}20 \text{ mmhr}^{-1}$34

Figure 18 The 10th and 90th percentile values of the droplet number concentration from 100-300 m a.g.l. based on measurements by the MRR at Bergen during 2019.34

Figure 19 Mean droplet-size distribution in the winter, spring, summer and autumn based on measurements at 100-300 m a.g.l. using the MRR at Bergen during 2017-2019, inclusive (left). The cumulative probability distribution for $\text{RR} > 0.2 \text{ mmhr}^{-1}$ based on the same data set. For legibility the x-axis has been truncated to only show RR of $1\text{-}20 \text{ mmhr}^{-1}$34

Figure 20 Background: Countries that have either more than 5 GW of wind energy installed capacity (IC) onshore or more than 1.5 GW offshore (as of end of 2020) (data from the GWEC 2020 status report (GWEC 2021). Countries shaded in black have a total IC of 50-300 GW, in blue 10-50 GW, in yellow 5-10 GW and in green 1-5 GW. The magenta dots indicate the locations for which long-term (> 1 year) of droplet size distributions are available.36

List of Tables

Table 1 IEA Wind Task 46 Participants during period 2021-2025.....	4
Table 2 A greatly abbreviated statement of example data availability for non-commercial purposes from tipping-bucket precipitation gauge measurements within national networks. This table focusses on countries from which droplet size distribution measurements are also available.....	16
Table 3 Typical relationships between reflectivity (Z, as derived from RADAR measurements, mm^6m^{-3}) and precipitation intensity (RR in mmhr^{-1}). Table adapted from (Collier 2000).....	19
Table 4 Z-R relationships by prevailing meteorology (see details at https://vlab.noaa.gov/web/wdtd/-/surface-precipitation-rate-sp-3 and (Dhiram and Wang 2016; Krajewski and Smith 1991))	19
Table 5 Examples of data availability for non-commercial purposes for RADAR measurements from national networks with a focus on countries from which droplet size distribution measurements are also available.	20
Table 6 The mean number concentrations of rain droplets expressed in number per cubic meter of air in a size class with a 1 mm diameter (i.e. $\# \text{m}^{-3} \text{mm}^{-1}$) of a given radius (either 1 mm or 2 mm) derived from the measurements shown in Figure 7-14 and the two theoretical distributions.....	32

Executive Summary

This report documents hydroclimatic parameters of importance to wind turbine blade leading edge erosion. The report opens by describing the importance of impacts from falling hydrometeors (rain droplets and hail stones) to leading edge erosion. A summary of the state of the science is provided regarding both hydrometeor size distributions as a function of rainfall rate and different measurement approaches available to capture key aspects of the hydroclimate. It is shown that hydroclimates and thus kinetic energy transfer to wind turbine blades due to hydrometeor impacts (used here as a proxy for materials stress) exhibits high variability across regions with either substantial wind resources and/or wind energy penetration. Meta-data for datasets available for describing the hydroclimate in regions with high wind turbine installed capacities are provided along with summary statistics from illustrative examples of those datasets. The report concludes by making a number of recommendations of key research priorities and identifying sites that will form the basis of future work under this IEA task.

1 Content and structure of this report

Wind turbine blade leading edge erosion is, to the first order, the result of material stresses caused by kinetic energy transfer from hydrometeors (e.g. hail and rain droplets, see full list of hydrometeors in Appendix A) impacting on the rotating blade*. Of the 11 classes of hydrometeors consisting of a full ensemble of particles (i.e. precipitation) defined by the World Meteorological Organization (WMO) the two of greatest interest in this work are rain (liquid droplets) and hail (particles of ice with diameters > 5 mm). The amount of kinetic energy transferred into the blade from falling hydrometeors is dictated by three primary factors:

- (i) The closing velocity between the hydrometeor and the blade.
- (ii) The number of hydrometeor impacts.
- (iii) The nature of the hydrometeors (size and phase).

Variations in wind turbine rotational speed dominate the closing velocity between falling hydrometeors and wind turbine blades. Availability of high-quality wind speed datasets has been addressed in previous IEA Wind Tasks (e.g. Task 36: <https://www.ieawindforecasting.dk/work-packages/work-package-1/task-1-1>). This report and the associated meta-data collection focus on the availability of data to describe the hydroclimate of different locations.

This report opens in section 2 by describing the primary meteorological drivers of wind turbine leading edge erosion. In the following section (section 3) a brief description of the primary metrologies available for making detailed measurements of precipitation intensity, hydrometeor size distributions and phase is provided. Section 4 describes the sites from which high-fidelity descriptions of precipitation intensity, hydrometeor size distributions and phase are available and summarizes key features of those datasets. Section 5 synthesizes the selection of priority areas on which future work will focus and that will form the basis for preliminary assessment of leading edge erosion potential will be made within this WorkPackage of IEA Wind Task 46. The final section, section 6, describes key conclusions and recommendations.

2 Identification of crucial meteorological parameters for wind turbine blade leading edge erosion

The amount of kinetic energy transferred into the blade from falling hydrometeors is dictated by three primary factors: (i) The closing velocity between the hydrometeor and the blade. (ii) The number of hydrometeor impacts. (iii) The nature of the hydrometeors (size and phase), plus (iv) the impaction efficiency. The following sub-sections describe these factors.

2.1 Closing velocity

The closing velocity between the rotating wind turbine blade and the falling hydrometeor is a function of:

* Once material damage occurs it can be amplified by other processes such as (1) UV radiation, freezing rain/ice coating and expansion and contraction of the blade coating due to variations in temperature and humidity and (2) physical and chemical corrosion due to dust and sea spray. These factors will be considered in future reports.

- 1) The hydrometeor fall velocity which is determined by the hydrometeor phase and diameter (Figure 1).

An approximation of the terminal velocity of rain droplets as a function of hydrometeor radius is:

$$V_{t,rain} = k \left[\frac{\rho_o}{\rho_{air}} R \right]^{1/2} \quad (1)$$

where R is the droplet radius (m), $k = 220 \text{ m}^{1/2}\text{s}^{-1}$, ρ_o is air density at sea level, ρ_{air} is air density at the altitude above sea level at which the rain droplet is crossing the rotor plane (Stull 2017).

An approximation of the terminal velocity of hail stones as a function of hydrometeor radius is:

$$V_{t,hail} = \left[\frac{8 |g| \rho_i}{3 C_D \rho_{air}} R \right]^{1/2} \quad (2)$$

where R is radius of the hail stone (m), ρ_i is the density of ice, ρ_{air} is air density at the altitude at which the hail is falling. $C_D=0.55$ is the drag coefficient (Stull 2017).

- 2) Wind speed and hence the rotational speed of the wind turbine blade (Figure 2).

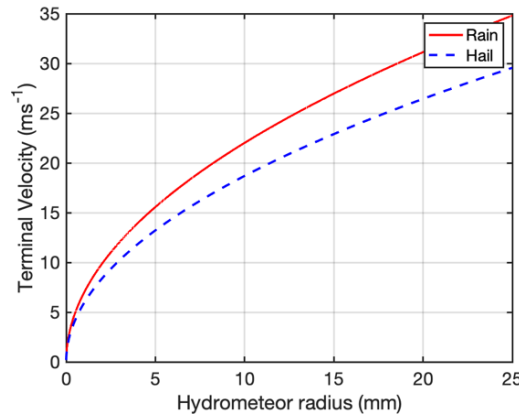


Figure 1 Terminal fall velocities for rain droplets and hail computed using Equations (1) and (2) and the following assumptions: $\rho_o = 1.225 \text{ kgm}^{-3}$, $\rho_{air} = 0.999 \rho_o$, $\rho_i = 900 \text{ kgm}^{-3}$.

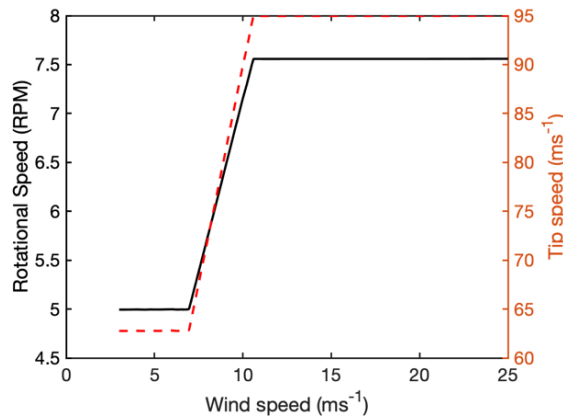


Figure 2 Illustrative example of wind turbine RPM and tip speed as a function of wind speed for the IEA 15 MW reference turbine (Gaertner et al. 2020). Power production begins at 4 ms^{-1} and ceases at wind speeds $> 25 \text{ ms}^{-1}$, thus no RPM or tip-speed data are plotted for wind speeds outside of the range of $4\text{-}25 \text{ ms}^{-1}$.

2.2 Size distributions of hydrometeors

Precipitation intensity is typically expressed in a depth of precipitation that would accumulate on the ground per unit time. It is thus usually presented in units of mm hr⁻¹. Precipitation intensity is a function of the diameter of the falling hydrometeors and their number concentration. The size distribution of hydrometeors dictates the number of impacts from falling hydrometeors, the mass of the droplets, plus their fall velocity and hence the kinetic energy transfer.

A number of different formulations have been derived to describe the rain droplet and hail stone spectra. The Marshall-Palmer distribution is often used in atmospheric science to describe the size distribution of liquid hydrometeors (rain droplets) (Marshall and Palmer 1948). It is based on data collected in Montréal, Canada in 1948. In it the number of droplets above radius, R , per cubic meter of air (N , m⁻³) is given by;

$$N = \frac{N_0}{\Lambda} e^{-\Lambda R} \quad (3)$$

Where $\Lambda = 8200(RR)^{-0.21}$ (m⁻¹), RR is the rainfall rate in mmhr⁻¹, and $N_0 = 1.6 \times 10^7 \text{m}^{-4}$. Example rain droplet size distributions derived using Eq (3) are shown in Figure 3 for RR of 1-46 mmhr⁻¹.

The DNV Recommended Practice issued in December 2020 (DNVGL 2020) for leading edge erosion testing proposes use of the so-called Best rain droplet size distribution. This distributional form was published in 1950 and is based on measurements made in the United Kingdom using filter paper (Best 1950). It has the form:

$$N = \frac{W}{V} \left(\frac{k \cdot d^{k-1}}{a^k} \right) e^{-|d/a|^k} \quad (4)$$

Where V is the spherical volume of the droplet, d is the droplet diameter, W is the total water volume, given by $67 \times RR^{0.846}$, RR is the rainfall rate in mmhr⁻¹, $k = 2.25$, $a = 1.3 \times RR^{0.232}$. Example rain droplet size distributions derived using Eq (4) are shown in Figure 4 for RR of 1-46 mmhr⁻¹.

Fewer studies have examined the size distribution of hail stones. Most proposed forms of the size distribution, like those for rain droplets, follow an exponential form with diameter (D , or radius, R) (Straka et al. 2000):

$$N(D) = n_0 \exp(-D\lambda) \quad (5a)$$

Others have postulated that the size distribution of hail (and rain droplets (Ulbrich and Atlas 1998)) follow a gamma distribution:

$$N(D) = n_0 D^\mu \exp(-D\lambda) \quad (5b)$$

Where in both cases n_0 is the intercept at $D = 0$, and μ and λ are additional fitting parameters.

Yet others have postulated that the size distribution of hail follows a power law distribution with parameters a and b :

$$N(D) = aD^b \quad (5c)$$

The simplest forms use a single fitting parameter, e.g.:

$$N(D) = 115\lambda^{3.63} e^{-\lambda D} \quad (6)$$

Where D is the hail stone diameter (Cheng and English 1983). And λ is fitting parameter.

Although theoretical distributions are most commonly formulated in terms of the number of droplets above some threshold radius (or diameter), observations of hydrometeors do not correspond to counts at specific infinitely narrow radii and thus are typically expressed

(as herein) as a number density (number per cubic meter of air) at a given radius or diameter in a class of diameters from D to $D+\Delta D$. It is convention to normalize such that $\Delta D = 1$ mm. Droplet size distributions (DSD) thus express the number concentrations of raindrops per cubic meter as a function of their diameter normalized for a fixed size interval (dN/dR or dN/dD , $\#m^{-3}mm^{-1}$).

The differences between rain DSD from the Marshall-Palmer, Best and other formulations are a function of RR and are most strongly manifest at larger droplet diameters that are infrequently observed. However, the differences are also evident at smaller (commonly observed) diameters. As an illustration of the differences in these two representations of the droplet size distribution, for a rainfall rate (RR) of 21 mmhr^{-1} , droplets with a radius of 1 mm are 3 times more abundant in the Marshall-Palmer distribution than in Best (Figure 3, Figure 4). For that same RR, droplets with a radius of 2 mm, are almost twice as abundant in the Best size distribution (Figure 3, Figure 4). These differences emphasize the key importance of investment in direct measurements of droplet size distributions using the technologies described in section 3.

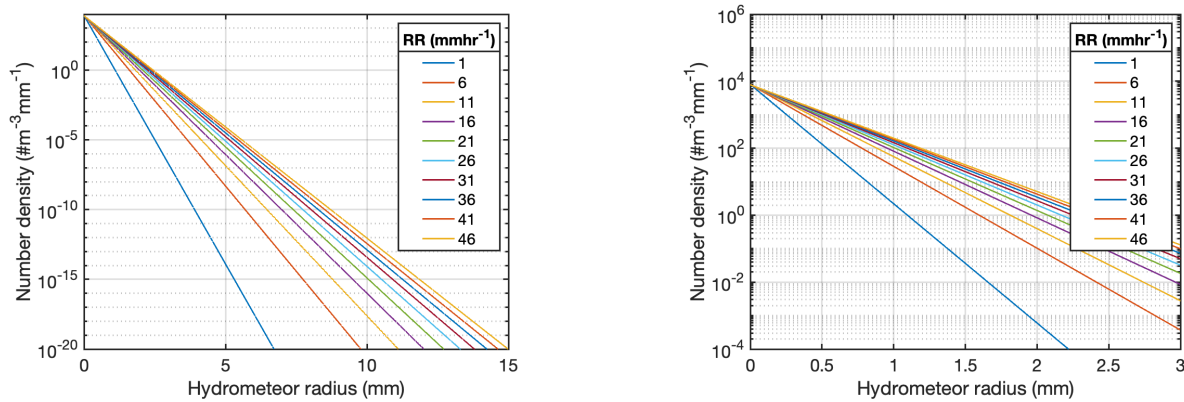


Figure 3 Illustrative example of the number size distribution of raindrops for different rainfall rates (RR) as described using the Marshall-Palmer size distribution (Eq. 3). The left panel shows hydrometeor radii of 0-15 mm, while the panel on the right confines the radii to 0-3 mm.

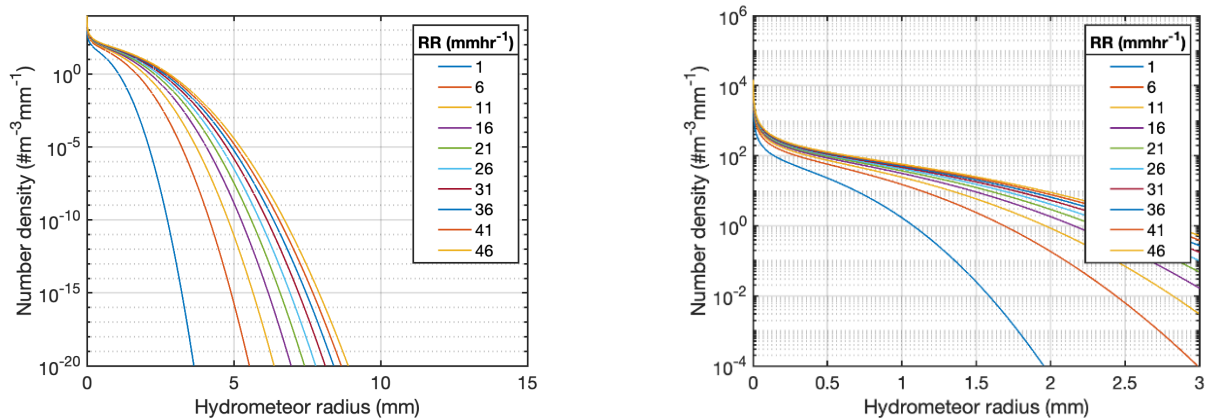


Figure 4 Illustrative example of the number size distribution of rain droplets for different rainfall rates (RR) as described using the Best size distribution (Eq. 4). The left panel shows hydrometeor radii of 0-15 mm, while the panel on the right confines the radii to 0-3 mm.

2.3 Precipitation phase

The precipitation phase not only dictates the size distribution of hydrometeors (Eq 3-6) and their fall velocities (Figure 1) but also the materials response to impacts. As described in a previous review (Keegan et al. 2013): First, the hail stone by definition is larger than 5 mm diameter thus greater in size than most rain droplets. Second, the fall velocity of hail stones is typically higher than for rain droplets so the impact speed with the blade is higher for hail stones. Furthermore, since hail stones are rigid thus less kinetic energy is dissipated by ‘splash’, although the behavior of hail can be either ductile or brittle manner dependent upon the strain rates and material responses, and will therefore vary as a function of material strain rate sensitivity. Materials response is a focus for WorkPackage 5 in this IEA Wind Task 46.

2.4 Impingement efficiency of hydrometeors on the leading edge

The impingement efficiency (i.e. mass flux of water impinging on a surface normalized by the freestream mass flux) (Heinrich et al. 1991) plays a key role to determine the mass of particles reaching the blade from the particle mass concentration in the air and the upstream velocity of particles relative to the blade. Most research suggests that for hydrometeor diameters above approximately 0.5 mm, the hydrometeors have sufficient inertia to ensure impaction on the blade and are not deflected by streamline deformation around the blade (Eisenberg et al. 2018; Li et al. 2020). The actual impact speed of hydrometeors is governed by the balance of particle momentum and aerodynamic forces. Small particles experience large decelerations when they reach the stagnation region close to the leading edge. The trajectory and speed of larger, more massive particles are less affected by the stagnation region in the vicinity of the leading edge. Figure 5 presents the ratio of impact speed to upstream speed for three particle densities for a closing velocity of 80 ms^{-1} based on from lagrangian tracking of spherical particles in a bidimensional computational fluid dynamics (CFD) simulation of a representative wind turbine airfoil (Prieto and Karlsson 2021). Water droplets with a diameter of 0.5 mm hit the leading edge at 95% of the upstream speed. Water droplets with a diameter of 0.025 mm impact the blade at 47% of the upstream speed (Figure 5).

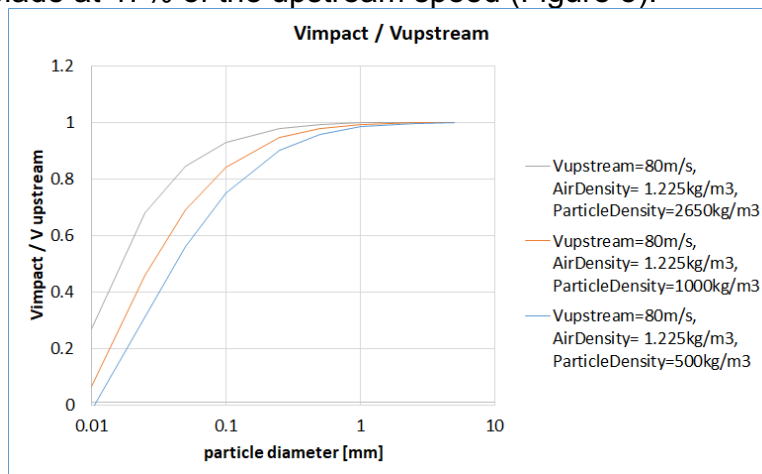


Figure 5 Ratio of impact speed to upstream speed for particles impinging on a blade.

The aerodynamics of the hydrometeor also plays a role: snowflakes have a much larger drag coefficient compared to droplets with the same mass. As a result, they experience higher deceleration in the stagnation region near the leading edge.

3 Measurement approaches

A range of measurement technologies are available for characterizing precipitation received at a given location. These metrologies are briefly described here.

3.1 Direct in situ measurement technologies

3.1.1 Tipping bucket rain gauges

The most widely used technology for quantifying precipitation in onshore national meteorological measurement networks is tipping bucket rain gauges. These gauges provide relatively high frequency (time-resolved) data regarding the accumulated height of liquid precipitation (i.e. solid hydrometeors are melted in many of these systems). They are thus useful in providing information regarding precipitation intensity, are available from a large number of stations (Table 2), but do not provide information regarding the phase or droplet size distribution. Most national meteorological networks use heated tipping-bucket gauges for measurements of liquid-equivalent precipitation accumulation over a time interval (Tokay et al. 2010). Some additionally equip these gauges to reduce under-catch (particularly of snow) under high wind conditions (Kochendorfer et al. 2020). In the USA the Frise heated tipping bucket gauge is the standard liquid precipitation accumulation gauge used at the approximately 900 stations that form the Automated Surface Observing System (ASOS) network.

Table 2 A greatly abbreviated statement of example data availability for non-commercial purposes from tipping-bucket precipitation gauge measurements within national networks. This table focusses on countries from which droplet size distribution measurements are also available.

Country	# sites	Data access	Period	Ancillary data
USA	>900	https://www.ncdc.noaa.gov/data-access/land-based-station-data/land-based-datasets/automated-surface-observing-system-asos	Since 2001	Wind speed at 10-m a.g.l., Icing (Freezing rain)
Denmark	31	https://www.dmi.dk/kontakt/frie-data/ (interface in Danish)		Wind speed at 10-m a.g.l.
Ireland	25+	https://www.met.ie/climate/available-data/historical-data	Most > 20 years	Wind speed at 10-m a.g.l.
Norway	667	https://seklima.met.no/	Most > 30 years	Wind speed at 10-m a.g.l.
Germany	>1000	https://www.dwd.de/EN/ourservices/opendata/opendata.html	Most > 30 years	Wind speed at 10-m a.g.l.

3.1.2 Disdrometers

Disdrometers measure the drop size distribution of precipitation (i.e. the number of droplets in a given size interval that fall during a specific time interval) and the fall velocity of the hydrometeors. Disdrometers thus provide information for the properties of greatest relevance of leading-edge erosion. The greatest disadvantage of disdrometers is that they generate point measurements at a given location. Further, such instruments are not

typically present in standard national weather service stations. Hence the spatial coverage of data from disdrometers is extremely limited.

A range of disdrometer designs are available (Kathiravelu et al. 2016). Two-dimensional video-disdrometers (VDIS) comprises two video cameras with perpendicular lines of sight. Objects passing through the measurement area obstruct the light and are detected as shadows by the cameras (Raupach and Berne 2015; Thurai et al. 2017). Impact disdrometers work by recording the kinetic energy transferred due to the impact of a falling hydrometeor on a detector (Tokay et al. 2001). Acoustic disdrometers work by detecting the acoustic signal generated by raindroplet impacts on a diaphragm (Kathiravelu et al. 2016). Most current generation disdrometers employ infrared beams over a short pathlength (of approximately 20 cm) and are referred to as optical disdrometers.

Disdrometer data typically comprise counts of droplets in different diameter classes. The process of translating those to number density normalized by the diameter range covered in a given class is shown in Equation (7) using the example of the 2nd generation OTT Parsivel (Parsivel²) disdrometer (Tokay et al. 2014):

$$N(D_i) = \frac{n_i}{F \times t \times v(D_i) \times \Delta D_i} \quad (7)$$

Where; n_i is the number count in diameter class i (D_i in mm), F is the area field of view of the disdrometer (0.0054m^2 for the OTT Parsivel² disdrometer), t is the sampling interval (in seconds, typically 30, 60 or 300 seconds), $v(D_i)$ is the fall velocity of a drop of that diameter (ms^{-1}), ΔD_i is the width of the size class (mm). $N(D_i)$ thus has units of the number per cubic meter of air per mm. Assuming spherical droplets the precipitation rate (RR) can be computed using:

$$RR = \frac{\pi}{6} \times \frac{3.6}{10^3} \times \frac{1}{F \times t} \times \sum n_i D_i^3 \quad (8)$$

The resulting RR has units of mmhr^{-1} .

Brief descriptions of the different commercially available disdrometers from which data are presented herein are given below:

A Campbell Scientific Inc. Present Weather Sensor (PWS) is a laser-based automatic weather station, employing an arrangement of two to three optical units to derive precipitation classification and intensity, drop size distribution and visual range. The optical units, comprising of a laser diode and a number of optical elements, produce light sheet patterns which extend between the sensors to detect hydrometeor size and distribution[†]. Collection algorithms can use environmental conditions captured by the PWS or nearby sensors, such as visibility, dew point and cloud ceiling to clean the data and determine which non-precipitation signals can be safely eliminated. As with all similar devices, a weakness of the PWS is the presence of non-precipitation noise inherent to the optical data collection (blowing dust and snow, insects in the detection range, spider webs, etc.), which can obscure the signal (Wade, 2003).



The OTT Parsivel-2 and Thies Laser Precipitation Monitor (LPM) disdrometers work on a similar measurement principle and measure hydrometeors as they fall through, and thus break, a series of adjacent horizontal beams. The Thies disdrometer uses a wavelength of 785 nm, while the OTT Parsivel² uses radiation with a wavelength of 650 nm. The

[†] The Campbell Scientific PWS100 Present Weather Sensor has been withdrawn from service.

specific instrument design and manufacturer determine the diameter classes covered (Tapiador et al. 2017). All systems use a variable class width as a function of diameter. The Theis laser disdrometer used in the UK DiVeN experiment employs 20 diameter classes (diameters) from ≥ 0.125 mm to > 8 mm (Pickering et al. 2019) and 20 velocity classes from 0 m to 10 m s^{-1} . For the OTT Parsivel² disdrometer the measured classes range from mid-point diameters of 0.0619 to 24 mm (in 32 classes) and 32 velocity classes from 0.2 to 20 m s^{-1} . Some disdrometers detect and report the occurrence of hail. It is frequently encoded in the data output using the WMO synoptic present weather code 89 (see Appendix for a complete listing of present weather codes).

3.1.3 Hail sensors

Direct hail measurements are also very sparse. Indeed, most meteorological networks operated by meteorological services do not directly measure the presence of hail and/or graupel. For example, at the US NWS ASOS sites there is a present weather sensor deployed (a Viasala light emitting diode weather identifier, LEDWI) that measures precipitation type using scintillation and thus can differentiate snow and rain. No automated sensors have been deployed (as 2021) for detection of hail and/or ice pellets, thus such reports are made by human observers and as such can only be made at approximately half of the approximately 900 ASOS stations that are currently subject to full-time augmentation by observers. The remainder operate largely autonomously.

Hail pads are a simple metrology for hail detection and sizing and are frequently used in community-based networks such as the Community Collaborative Rain, Hail and Snow network (CoCoRaHS) in the USA, Canada and Bahamas (Reges et al. 2016), the Association Nationale d'Etude et de Lutte contre les Fléaux Atmosphériques (ANELFA) in France (Berthet et al. 2011) and the Croatian network (Počakal et al. 2009). Hail pads in the CoCoRaHS network are made of Styrofoam blocks wrapped in heavy duty aluminum foil. After a hail event they are visually inspected for hail markings to provide a count of hail impacts and are measured to estimate the hail diameter. This is highly labor-intensive and the resulting data are somewhat subjective.

Recently automated hail sensors have been developed. One purpose-built automated hail sensor that is currently commercially available is the ISAW HailFlow 4. It samples both the presence of hail (as in the disdrometers described above) and also characterizes hail stone size. The sensor uses an acoustic measurement principle, where impacts of hail stones induce a measurable change in internal acoustic pressure.

3.2 Remote sensing technologies

3.2.1 RADAR

Single polarization scanning RADAR form the basis of national RADAR networks around the world. They are active remote sensing instruments that emit radiation (at wavelengths of a few centimeters) into the atmosphere and detect the portion that is backscattered to the antenna. They are used to derive precipitation intensity using Z-R relationships that link the reflectivity (intensity of reflected radiation) as measured by the RADAR to rainfall rate (RR) in mmhr^{-1} (Wilson and Brandes 1979).

RADAR reflectivity (Z) is strongly dependent on the size distribution of hydrometeors in clouds. Z is a function of the number (N) and droplet diameter (D) (or radius) raised to the

sixth power of hydrometeors in the atmospheric volume (vol) that is hit by the RADAR beam:

$$Z = \frac{\sum_1^N D^6}{vol} \quad (9)$$

Since hydrometeor number and size distributions vary according to the cloud type being sampled, Z-R relationships also vary according to the prevailing meteorological conditions and precipitation type (Table 3 and Table 4).

Table 3 Typical relationships between reflectivity (Z, as derived from RADAR measurements, mm⁶m⁻³) and precipitation intensity (RR in mmhr⁻¹). Table adapted from (Collier 2000).

Equation (Z = f(RR))	Precipitation type
104RR ^{1.5}	Drizzle
250RR ^{1.5}	Widespread rain
200RR ^{1.6}	Stratiform rain
31RR ^{1.71}	Orographic rain
500R ^{1.5} or 486RR ^{1.37}	Convective (Thunderstorm) rain
2000RR ^{2.0}	Aggregated snow
1780RR ^{2.21}	Snow

Table 4 Z-R relationships by prevailing meteorology (see details at <https://vlab.noaa.gov/web/wdtd/-/surface-precipitation-rate-sp-3> and (Dhiram and Wang 2016; Krajewski and Smith 1991))

RELATIONSHIP	Recommended for:
Marshall-Palmer: (Z=200R ^{1.6})	General stratiform precipitation
East-Cool Stratiform: (Z=130R ^{2.0})	Winter stratiform precipitation - east of continental divide Orographic rain - East
West-Cool Stratiform: (Z=75R ^{2.0})	Winter stratiform precipitation - west of continental divide Orographic rain - West
WSR-88D Convective: (Z=300R ^{1.4})	Summer deep convection Other non-tropical convection
Rosenfeld Tropical: (Z=250R ^{1.2})	Tropical convective systems

To derive rainfall rate from radar measurements one has to first convert from the measured property (RADAR return, DX in dBZ) to radar reflectivity (Z):

$$Z = 10^{DX/10} \quad (10)$$

And then from RADAR reflectivity (Z) to rainfall rate using appropriate scaling factors (a and b, Table 4) for the given meteorological context:

$$RR = \left(\frac{Z}{a}\right)^{1/b} \quad (11)$$

For a Marshall-Palmer distributed hydrometeor population the Z-R relationship is given by: $Z = 200RR^{1.6}$ which is given in Table 4 as appropriate for stratiform rain.

For RADAR using a 10 cm wavelength of radiation (as typifies the RADAR network in the USA), hail in clouds is associated with extremely high RADAR returns. This threshold is frequently assumed to be ≈ 45 dBZ (Witt et al. 1998). Thus, single polarization scanning Doppler RADAR can be used to provide spatial patterns of RR and an index of hail occurrence. In the USA the RADAR network, data are available within a scanned radius of 230 km with a repeat time of ~ 5 -10 minutes.

An estimate of reflectivity can also be calculated from disdrometer measurements using:

$$Z = \frac{\sum_1^j D_i^6 n_i}{v_t(D_i) dt A} \quad (12)$$

Where j is the number of size classes, D_i is the midsize diameter of the i^{th} size class, n_i is the number of hydrometeors in the i^{th} size class, $v_t(D_i)$ is the terminal fall velocity of raindrops of size D_i , dt is the sampling interval and A is the field of view of the disdrometer. Reflectivity (in dBZ) is derived from the units of mm^6m^{-3} by taking the logarithm in base-10 and multiplying by 10 (Tokay et al. 2009).

3.2.2 Dual-polarization RADAR

Dual polarization RADAR provide information regarding precipitation intensity (as in the single polarization RADAR) but via use of horizontally polarized and vertically polarized RADAR beams also obtain information regarding the hydrometeor aspect ratio (the degree to which the hydrometeors reflecting the beam are spherical). Larger magnitude differential reflectivity for the vertical and horizontal polarized beams (Z_{VH}):

$$Z_{VH} = 10 \times \log \left(\frac{Z_{HH}}{Z_{VV}} \right) \quad (13)$$

And larger linear depolarization ratios (L_{DR}):

$$L_{DR} = 10 \times \log \left(\frac{Z_{VH}}{Z_{HH}} \right) \quad (14)$$

Where Z_{HH} = reflectivity in horizontal, and Z_{VV} =reflectivity in vertical, are associated with non-spherical hydrometeors. Because rain droplets deform and flatten as they fall while hail particles do not, hail tends to be more spherical and thus to be associated with lower Z_{VH} values (Herzogh and Jameson 1992; Straka et al. 2000). Algorithms for detection of hail and estimation of the 75th percentile hail diameter from scanning dual polarization RADAR have been developed and experimentally evaluated (Wallace et al. 2019).

Many countries have upgraded their national RADAR networks to dual polarization (Table 5). For example, the USA has a network of 159 dual polarization RADAR operating since 2013. As of 2021 the Canadian Weather RADAR Network (CWRN) comprises 31 stations with full 'conventional' reflectivity for ranges of upto 250 km and dual-polarization to 120 km range (Wijayarathne and Coulibaly 2021).

Scanning dual polarization RADAR thus provide information regarding the spatial patterns of RR and hail (and other hydrometeors). Such data, along with the radial velocity (wind speed) measurements from the Doppler frequency shift have been used with assumed hail and rain droplet size distributions to derive first-order estimates of kinetic energy transfer to wind turbine blades at selected sites across the USA (Letson et al. 2020b).

Table 5 Examples of data availability for non-commercial purposes for RADAR measurements from national networks with a focus on countries from which droplet size distribution measurements are also available.

Country	# sites	Data access	Single or dual polarization	Data or visualization
USA	159	https://www.ncdc.noaa.gov/data-access/radar-data	Dual as of 2013	Data
Canada	31	https://climate.weather.gc.ca/radar/	Dual	Visualization
Ireland	2	https://data.gov.ie/dataset/rainfall-radar	Dual	hdf5 5 min frequency.
Norway	11	https://thredds.met.no/thredds/catalog/remote_sensing/reflectivity-nordic/catalog.html	Dual	Data

3.2.3 Micro-rain RADAR

Micro-rain RADAR (MRR) are active, vertically pointing remote sensing systems that can provide drop-size distributions of hydrometeors at high sampling rates (every 10 s) (Klugmann et al. 1996; Löffler-Mang et al. 1999). In contrast to disdrometers, which provide similar observations from a small measurement volume at the instrument's observation level, MRR remotely sense vertical profiles of hydrometeor properties up to several kilometers above the instrument and thus spatially averaged over a much larger measurement volume. The MRR measurement principle is similar to that of the scanning RADAR described above, in that it relies on scattering of electromagnetic waves emitted by the instrument and then scattered back to the RADAR antenna by hydrometeors. By analyzing the Doppler shift of the backscattered signal the vertical fall velocity of the hydrometeors can be determined. Since the fall velocity of hydrometeors scales with their size and the strength of the signal with the number of hydrometers, the size distribution can be computed. In addition, other relevant parameters, such as, RADAR reflectivity, rain rate can be computed.

3.2.4 Satellite-derived products

A range of satellite-derived products have been developed that seek describe precipitation rates and in cloud hydrometeor phase (Hashemi et al. 2020). The Tropical Radar Measuring Mission (TRMM) was in operation from 1997 to 2015 providing precipitation for tropical and sub-tropical regions. NASA provides Level 1 to Level 3 products for this period <https://gpm.nasa.gov/data/directory>. NASA also provides access to the Global Precipitation Measurement (GPM) (Skofronick-Jackson et al. 2018) which is an international network of satellites to provide next-generation global observations of rain and snow (https://www.nasa.gov/mission_pages/GPM/main/index.html). The most processed (Level 3 data) include IMERG Final Run at a resolution of approx. 10 km available from the year 2000 onwards. This is a merged data set which uses satellite microwave precipitation estimates, together with microwave-calibrated infrared (IR) satellite estimates, precipitation gauge analyses, and potentially other precipitation estimators at fine time and space scales for the TRMM and GPM eras over the entire globe. Other data can also be accessed such as 3B combined which uses the GPM Combined Radar-Radiometer Algorithm to provide high resolution estimates of surface rainfall rate and precipitation vertical distributions and 3A Radar and Radiometer but these are slightly coarser resolution 0.25 degree/daily. It is also possible to access Level 1 and 2 data but these are single platform i.e. less integrated measurements and require more processing.

3.2.5 Gridded data sets

A range of global and regional reanalysis products have been developed to provide a spatial homogeneous description of past weather and climate conditions. These gridded products are blend of observations with past short-range weather forecasts performed with state-of-the-art numerical models. One of the highest-resolution and most recently developed of these is the ERA5 reanalysis developed by the European Centre for Medium/Range Weather Forecasts (Hersbach et al. 2020). This reanalysis product has a range of characteristics that make it potentially useful for assessment of leading edge erosion potential:

- 1) The range and quality of data assimilated is unprecedented.

- 2) Output is available at a disjunct frequency of 1 hour for many atmospheric properties and at a horizontal grid spacing of approximately 30 km. It includes; a) Wind speeds at both 10 m and 100 m a.g.l., b) hourly precipitation rate, plus ancillary variables of relevance including; specific humidity, radiation.
- 3) It has been shown to exhibit some skill for annual accumulated precipitation, although biases of up to +/-200 mm/year were found for parts of North America (Tarek et al. 2020). It also exhibits some fidelity with respect to wind speeds (Jourdier 2020), though a large negative bias was found in mountainous areas of North America (Pryor et al. 2020).

Output from the ERA5 reanalysis has been employed in prior analyses of LEE potential (Letson et al. 2020c; Prieto and Karlsson 2021). Caution must be applied in interpreting the results because of the absence of modeled droplet size distributions, hydrometeor phase and local intensification of precipitation particularly under convective conditions that occurs at scales vastly below those represented in the ERA5 reanalysis model.

Hindcast products are also being generated. NORA3 is a hindcast product for the North Sea, the Norwegian Sea and the Barents Sea and adjacent land areas with a horizontal resolution of 3 km, generated by the Norwegian Meteorological Institute (Haakenstad et al. 2021). It is currently available for 2004-2018, but is being extended both forward and back in time. NORA3 is based on the nonhydrostatic numerical weather prediction model, HARMONIE-AROME, and is run to downscale the ERA5 reanalysis data set. Due to its rather high horizontal resolution, and its improved grid-resolving coastlines, NORA3 performs, much better than the previous Hindcast (NORA10) or ERA5 particularly in complex terrain and in the coastal areas,. First comparisons with lidar wind profile measurements at different onshore and offshore locations show an excellent agreement (Figure 6). There is potential that, in the absence of co-located wind measurements, NORA3 winds could be used in combination with direct measurements of droplet size distributions for LEE quantification. NORA3 wind profiles over the rotor disk of state-of-the art wind turbines may provide more accurate information than those derived by extrapolating wind speed observations from 10 m height. An analysis and validation of hydrometeor information in NORA3, in particular with respect to droplet size distributions, that can be realized by a systematic comparison with disdrometer or MRR measurements, is pending.

3.2.6 Numerical Weather Prediction models

There are efforts underway to enhance NWP model fidelity with respect to precipitation phase and potentially droplet size distributions. Such work is essential to development of a priori estimates of wind turbine blade leading edge erosion potential over large areas, but such work is nascent. Current research is actively exploring sensitivity analyses focused on improved understanding of the performance as a function of model configuration (e.g. microphysics parameterizations) and resolution. Much of this work in the USA is focused on high-impact deep convection (Labriola et al. 2019). Very few studies have examined the potential to use direct output from models such as the Weather Research and Forecasting (WRF) model to develop a priori estimates of leading edge erosion potential (Letson et al. 2020a).

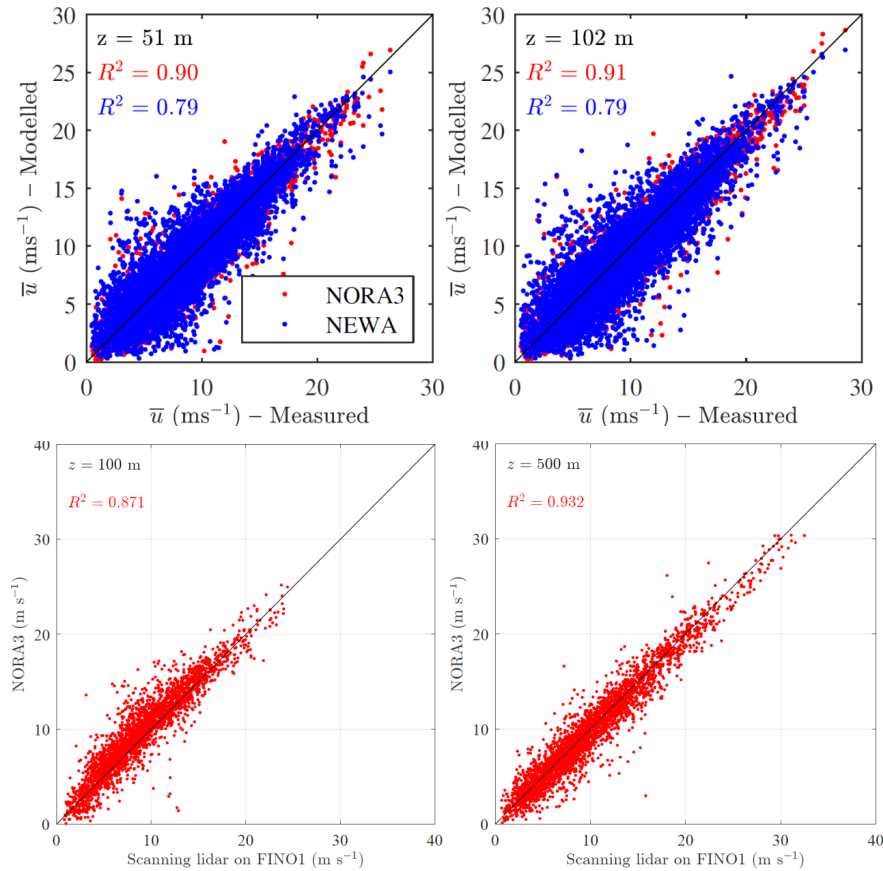


Figure 6 Evaluation of NORA3 wind speeds. Upper panels show hourly mean wind speed at 50 m (left panel) and 100 m (right panel) from NORA3 and the New European Wind Atlas (NEWA) compared to cup anemometer measurements from the FINO1 platform in the North Sea for the year 2009. Lower panels show the mean wind speed at 100 m (left panel) and 500 m (right panel) from NORA3 compared to lidar wind profiles measured with a Leosphere WindCube 100S at the FINO 1 platform during the OBLEX-F1 campaign in 2015 and 2016.

4 Data availability for use in mapping wind turbine blade leading edge erosion potential

Accompanying this report is a spreadsheet containing metadata for key data sets of high value to describing leading edge erosion potential; those deriving from long-term deployments of disdrometers, MRR and/or hail sensors (Appendix B, doi: 10.5281/zenodo.5648211). In section 4.1 we describe the sites from long-term droplet size distributions are available (section 4.1). In section 4.2 we provide illustrative examples of droplet size distributions from selected instruments at those sites.

4.1 Hydrometeor size distribution measurements: Locations

4.1.1 Norway

Since 2010 the Geophysical Institute at the University of Bergen, Norway (GFI/UiB) has operated a METEK MRR, mainly on the rooftop observational platform of the main institute building (60.38°N and 5.33°E at an altitude of 39 m a.m.s.l.). The site is co-located with a basic synoptic station of the Norwegian Meteorological Institute (Bergen-Florida, WMO number: 01317) and during the past 4 years parallel droplet size

distribution measurements by an OTT-Parsivel disdrometer are available. The site is characterized by a marine West Coast climate with moderate summer temperatures and for the latitude relatively mild winters. The average annual precipitation amount is 2250 mm with the highest precipitation amounts during autumn and winter. Winter temperatures fall below zero typically only for short periods. There are rare occasions of freezing rain, but heavy icing conditions are very rare. Graupel showers occur during all of the year, mostly in connection with frontal passages, hail events are extremely rare. The MRR was also deployed for about 8 weeks (February/March 2018) onboard the NATO Research vessel R/V Alliance in the Iceland-Greenland Sea (Renfrew et al. 2019).

4.1.2 Wind Energy Institution of Canada (WEICan)

The WEICan site is located at North Cape in Prince Edward Island Canada (47.035°N, -64.0154°E). It is an active wind generation site, comprised of five wind turbine generators and an 80-meter meteorological tower equipped with 15 anemometers, temperature sensors, barometers and wind vanes (Barthelmie et al. 2016). Of relevance to this study, a Campbell Scientific PWS100 precipitation sensor was operated at 11 meters on the tower, to record 1-minute resolution precipitation data from October of 2018 to December of 2020. Concurrent wind speed and direction data are available for the site. The WEICan site is a cool, humid maritime climate. The summers are temperate with consistent low wind with low-to-moderate levels of rainfall. The typical winters are well below freezing with heavy snowfall and high winds blowing off the ocean. Being a coastal site there is year-round exposure to marine aerosols. During the winter, and especially during late fall and early spring, freezing rain events are common, with icing events often shutting down turbine operations. Hail events are rare.

4.1.3 U.S. Department of Energy Atmospheric Radiation Measurement (ARM) sites

The U.S. Department of Energy (DoE) operates a number of ARM sites, including at a primary hub within the Southern Great Plains in north-central Oklahoma and southern Kansas. There are over 50 instrument platforms including the following that are key relevance to leading edge erosion; radiometers, RADARS, lidars, surface instrumentation including disdrometers. At the SGP central facility near Lamont, Oklahoma (OK) (36.6072°N, -97.4875°E) there are three disdrometers; impact disdrometer (February 2014 continuing), optical (Parsivel²) disdrometer (January 2006 – October 2021) and video disdrometer (January 2000 ongoing). Other long term disdrometer measurements at DoE facilities include:

- Billings, OK: 36.477116°N, -97.421081°E (November 2016 – ongoing)
- Barrow, AK: 71.3230°N, -156.6090°E (April 2017 - ongoing).

The southern Great Plains are subject to frequent deep convection and associated heavy rain and hail (Letson et al. 2020a; Letson et al. 2020b), but freezing rain is uncommon. The relative aridity of the landscape mean wind-blown dust may represent an important contributor to LEE. The occurrence of hail is encoded in the data output from the Parsivel² laser disdrometers using the WMO synoptic present weather code 89. This code was reported in 105 5-minute periods in the data from 2019 as collected at Lamont and in 83 5-minute periods in data from that same year collected at Billings (approx. 20 km away).

4.1.4 UK onshore

14 Thies laser precipitation monitors (LPMs) ran from February 2017 for approximately two years at locations around the United Kingdom as part of the Disdrometer Verification Network (DiVeN) project (Pickering et al. 2019). The climate of the UK is generally mild-maritime but there is notable variation in, for example, the frequency of deep convection and hail. The occurrence of hail is encoded in the data output using the WMO synoptic present weather code 89. This code was reported in 89 5-minute periods in the data from 2018 as collected at the DiVeN site in the Caringorms (Scotland) and in 17 5-minute periods in data from that same year collected at Reading in England.

4.1.5 Offshore waters of the UK

PWS100 Campbell Scientific have been installed at two different sites by ORE Catapult. In August 2018, two disdrometers were installed onto ORE Catapult's National Offshore Anemometry Hub (NOAH). The hub is located three nautical miles (5.56 km) from the coast of Blyth, Northumberland. One disdrometer was installed onto the existing platform at 25 m above sea level and the other mounted 55 m above sea level. A further PWS100 was installed in December 2020 at ORE Catapult's offshore Levenmouth Demonstration Turbine and is mounted at sea level near to the base of the tower. At both sites, measurements are recorded minutely and include rain droplet size distributions, rainfall rate, and hydrometeor classification and frequencies. Wind speed data is also available at both sites and radiometers are also installed at NOAH.

4.1.6 Denmark

Under the EROSION project Parsivel² disdrometers were deployed at two offshore locations; one the North Sea and one in the Baltic Sea and multiple onshore locations. At the Risø site three disdrometers were deployed; one at the ground near a tall meteorological mast, one at the top of the mast at height 123 m above ground level and the third at ground level 950 m south-southeast of the tall mast. In a related study data from multiple disdrometers in Germany located on the coast of the North Sea and Baltic Sea were used to characterize the variation in precipitation type, rainfall amount and kinetic energy for leading edge erosion and to examine the weather type dependence of the Z-R relationship (Tilg et al. 2021). As expected, Z-R relationships were consistent across sites but exhibit large variation with weather type.

4.1.7 Network operated by Orsted

OTT Parsivel² disdrometers were deployed at two offshore sites and one near-shore site, in Denmark (West coast – Horns Rev 2), Taiwan (Strait of Taiwan) and the United States (North-East coast). In Denmark, the disdrometer was installed on the roof of the offshore platform (at 25 m height), in Taiwan, on top of a met-mast (at 90 m height) and in the United States on top of a building (at 10m height). At all three sites, measurements are recorded every minute and include rain droplet size distributions, rainfall rate, and precipitation type. Wind speed data are available at the sites in Denmark and Taiwan.

4.2 **Examples of measured droplet size distributions**

In situ data from disdrometers show marked variability between different events and deviations from the droplet size distributions described above in section 2 (Dolan et al. 2018; Herring et al. 2020). To illustrate this variability from site to site, Figures 7-13

summarize the droplet size distributions measured using disdrometers/MRR deployed at sites across the globe. Note in all cases statements regarding the number of droplets at a specific radius (1 or 2 mm) have been interpolated from the native resolution of the instruments. All datasets have been conditionally sampled to generate droplet size spectra at different rainfall rates and for legibility, in all cases the radii considered range upto 3 mm and thus truncate the observational range of most disdrometers.

- Figure 7 shows the mean raindrop size distribution as measured in Bergen, Norway conditionally sampled by different rain rates. For intense rain ($15\text{-}30\text{ mm hr}^{-1}$), the mean droplet number density at between 100 and 300 m a.g.l. for a radius of 1 mm is $\sim 22\text{ m}^{-3}\text{mm}^{-1}$ and for a radius of 2 mm $0.22\text{ m}^{-3}\text{mm}^{-1}$. Note the droplets distributions at 100-300 m may not be equivalent to those that reach the ground.

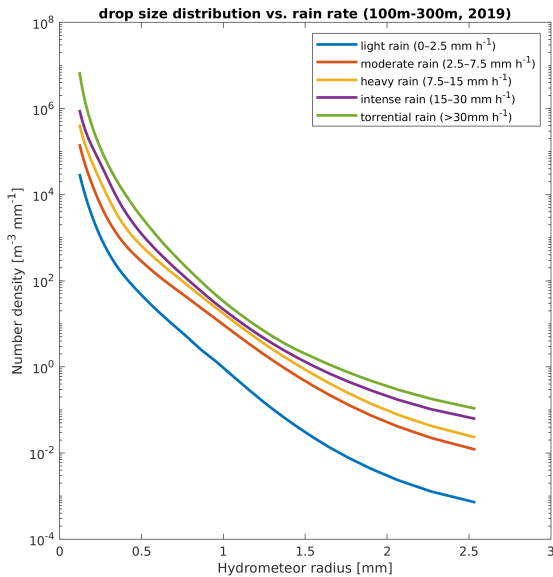


Figure 7 Mean droplet-size distribution measured by a micro-rain RADAR (MRR) between 100 m a.g.l. and 300m a.g.l. in Bergen Norway during the year 2019.

- Figure 8 shows the mean droplet-size distribution measured by the CSI Present Weather Sensor instrument at the Wind Energy Institute of Canada.

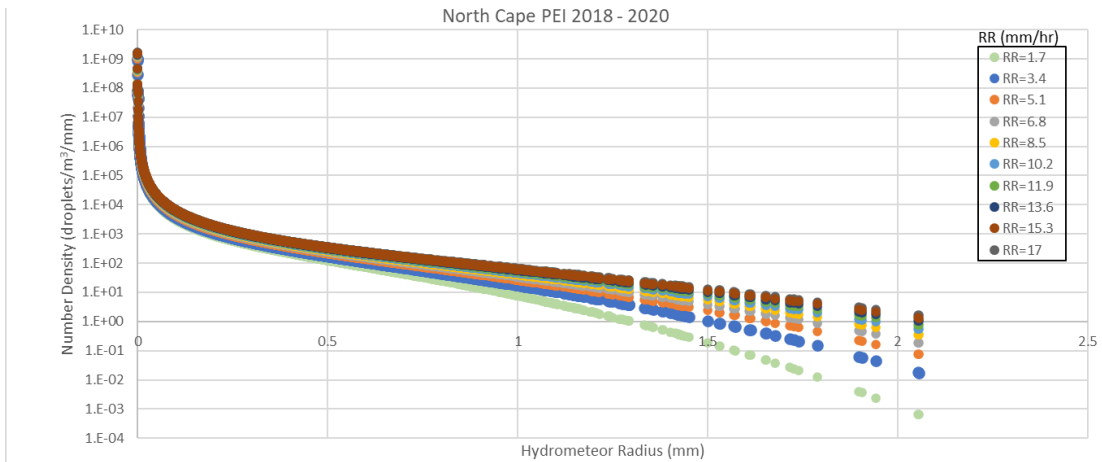


Figure 8 Droplet-size distribution measured by a Campbell Scientific PWS100, at an elevation of 11 meters at the North Cape wind farm in Prince Edward Island, Canada from October 2018 through December 2020. Note: No instances of $RR > 17\text{ mm hr}^{-1}$ are present in this dataset.

- 3) Figure 9 shows the mean droplet-size distribution measured by ground-based Parsivel² disdrometers at two DoE ARM sites in the Southern Great Plains during 2019. Figure 10 shows data for the same year from an impact disdrometer and a video disdrometer at the Lamont site for comparative purposes. There are some important differences in data from the different disdrometers and between these two sites and data from Europe. For example:
- a. At the Lamont station:
 - Based on data from the optical disdrometer: For a rain rate of 6-11 mmhr⁻¹ the number concentration of droplets of approx. 1 mm radius is 37 mm⁻³ mm⁻¹, while for a rain rate of 21-26 mmhr⁻¹ it is 81 mm⁻³ mm⁻¹. Equivalent concentrations for approximately 2 mm radii droplets are; 1.0 and 3.9 mm⁻³ mm⁻¹. This site has a high frequency of hail occurrence and 4.7% of 1-minute sampling periods exhibited non-zero precipitation. Using a threshold of RR > 0.2 mm hr⁻¹ as the threshold for non-zero precipitation, the 90th, 95th and 99th percentile precipitation rates from this disdrometer are; 6.6, 13.1 and 41.9 mmhr⁻¹. Thus 1% of periods when significant precipitation is observed have precipitation rates in excess of 41.9 mmhr⁻¹.
 - Based on data from the impact disdrometer: For a rain rate of 6-11 mmhr⁻¹ the number concentration of droplets of approx. 1 mm radius is 52 mm⁻³ mm⁻¹, while for a rain rate of 21-26 mmhr⁻¹ it is 129 mm⁻³ mm⁻¹. Equivalent concentrations for approximately 2 mm radii droplets are; 0.38 and 2.9 mm⁻³ mm⁻¹. This site has a high frequency of hail occurrence and 7% of 1-minute sampling periods exhibited non-zero precipitation. Using a threshold of RR > 0.2 mm hr⁻¹ as the threshold for non-zero precipitation, the 90th, 95th and 99th percentile precipitation rates from this disdrometer are; 8.1, 16.6 and 44.6 mmhr⁻¹. Thus 1% of periods when significant precipitation is observed have precipitation rates in excess of 44.6 mmhr⁻¹.
 - Based on data from the video disdrometer: For a rain rate of 6-11 mmhr⁻¹ the number concentration of droplets of approx. 1 mm radius is 41 mm⁻³ mm⁻¹, while for a rain rate of 21-26 mmhr⁻¹ it is 97 mm⁻³ mm⁻¹. Equivalent concentrations for approximately 2 mm radii droplets are; 0.4 and 2.65 mm⁻³ mm⁻¹. Using a threshold of RR > 0.2 mm hr⁻¹ as the threshold for non-zero precipitation, the 90th, 95th and 99th percentile precipitation rates from this disdrometer are; 7.9, 14.9 and 44.5 mmhr⁻¹. Thus 1% of periods when significant precipitation is observed have precipitation rates in excess of 44.5 mmhr⁻¹.
 - b. At the Billings station based on data from the Parsivel² disdrometer: For a rain rate of 6-11 mmhr⁻¹ the number concentration of droplets of approx. 1 mm radius is 36 mm⁻³ mm⁻¹, while for a rain rate of 21-26 mmhr⁻¹ it is 88 mm⁻³ mm⁻¹. Equivalent concentrations for approximately 2 mm radii droplets are; 0.6 and 2.9 mm⁻³ mm⁻¹. This site also has a high frequency of hail occurrence but the disdrometer data indicate a lower precipitation frequency with 4.2% of 1-minute sampling periods exhibiting non-zero precipitation. Using a threshold of RR > 0.2 mm hr⁻¹ as the threshold for non-zero precipitation, the 90th, 95th and 99th percentile precipitation rates from the disdrometer are; 6.9, 16.0 and 49.8 mmhr⁻¹. Thus 1% of periods when precipitation is observed have precipitation rates in excess of 49.8 mmhr⁻¹.

The differences in precipitation climatology at these two stations (Lamont v Billings), that are located only approx. 20 km apart, likely reflects spatial gradients in precipitation regimes (Letson et al. 2020c) and/or the importance of small-scale convective systems to the precipitation climate of the SGP (Letson et al. 2020a) the influence of which is highly impactful in a single year of observations. The difference between data collected using the optical, video and impact disdrometers at Lamont are illustrative of the challenges in comparing data across instruments (Johannsen et al. 2020; Sarkar et al. 2015; Tapiador et al. 2017).

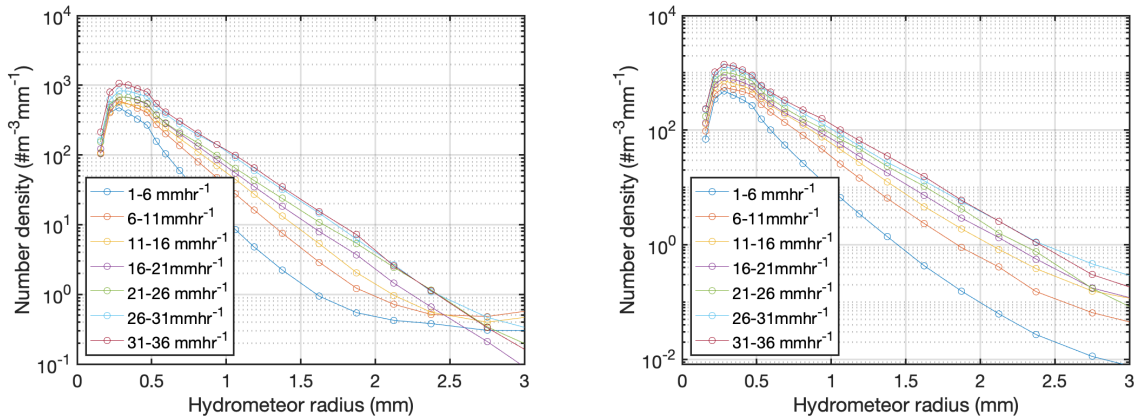


Figure 9 Mean droplet-size distribution measured by a ground-based Parsivel² disdrometers at the Lamont Southern Great Plains DoE ARM site (left) and the Billings Southern Great Plains DoE ARM sit (right) during the year 2019. Note the axes are different in the two frames and have been scaled to optimally present the data range at each site. Droplet size distributions are only shown for RR classes with > 50 data samples, but RR classes are represented by any data samples are included in the legend.

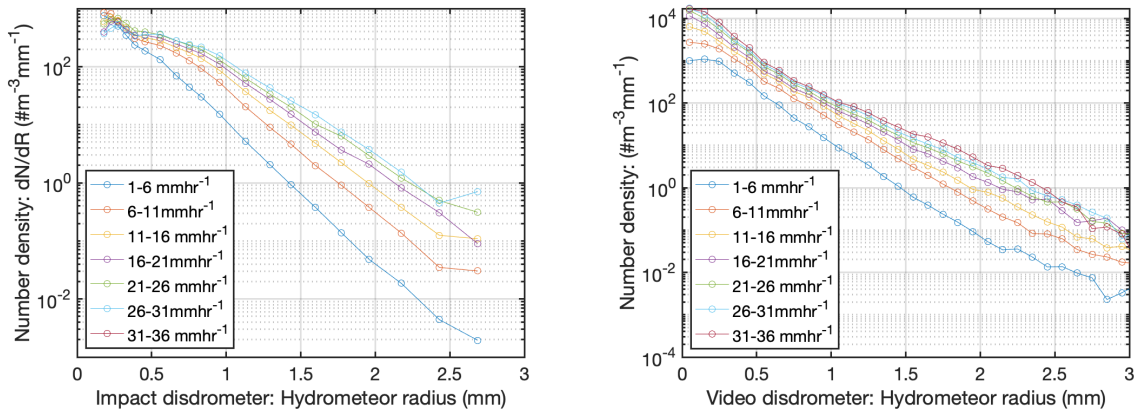


Figure 10 Mean droplet-size distribution measured by an impact disdrometer (left) and a video disdrometer (right) at the Lamont Southern Great Plains DoE ARM site during the year 2019. Droplet size distributions are only shown for RR classes with > 50 data samples, but RR classes are represented by any data samples are included in the legend.

- 3) Figure 11 shows the mean droplet-size distribution during 2018 as measured by ground-based disdrometer at three DiVeN experiment sites in the United Kingdom: the Cairngorm site (in Scotland), Reading in England and the Weybourne Atmospheric Observatory in the Norfolk coast of the North Sea.

- a. At the Cairngorm site for a rain rate of 6-11 mmhr⁻¹ the number concentration of droplets of approx. 1 mm radius is 21 mm⁻³mm⁻¹, while for a rain rate of 21-26 mmhr⁻¹ it is 42 mm⁻³ mm⁻¹. Equivalent number concentrations for approximately 2 mm radii droplets are; 2.2 and 5.0 mm⁻³mm⁻¹. The probability of precipitation based on a RR threshold of 0.2 mmhr⁻¹ is 13.4%. The 90th percentile RR for this threshold is 5.5 mmhr⁻¹, the 99th percentile value is 39.5 mmhr⁻¹.
- b. Data from Reading indicate very few observational periods with RR > 26 mmhr⁻¹. Only 63 sample periods with rainfall rates of 21-26 mmhr⁻¹ and fewer than 50 exceed 26 mmhr⁻¹. These data indicate for a rain rate of 6-11 mmhr⁻¹ the number concentration of droplets of approx. 1 mm radius is 21 mm⁻³mm⁻¹, while for a rain rate of 21-26 mmhr⁻¹ it is 71 mm⁻³mm⁻¹. Equivalent concentrations for approximately 2 mm radii droplets are; 0.2 and 1.1 mm⁻³mm⁻¹. RR > 0.2 mmhr⁻¹ were reported with a frequency of 6.3%. The 99th percentile RR (computed using a threshold of 0.2 mmhr⁻¹ to define significant precipitation), is 39.5 mmhr⁻¹. Thus significant precipitation is reported on half as many 1-minute periods at Reading as in the Cairngorms, and the 1% heaviest precipitation rates are half those reported at the Cairngorm site.
- c. Data from Weybourne also indicate very few reports of heavy precipitation. No RR classes above 12-21 mmhr⁻¹ are associated with sample sizes > 50. For a RR of 6-11 mmhr⁻¹ the number concentration of droplets of approx. 1 mm radius is 16 mm⁻³mm⁻¹, while for a rain rate of 21-26 mmhr⁻¹ it is 31 mm⁻³mm⁻¹. Equivalent number concentrations for approximately 2 mm radii droplets are; 1.4 and 3.2 mm⁻³mm⁻¹. The frequency of 1-minute RR > 0.2 mmhr⁻¹ is, like Reading, 6%.

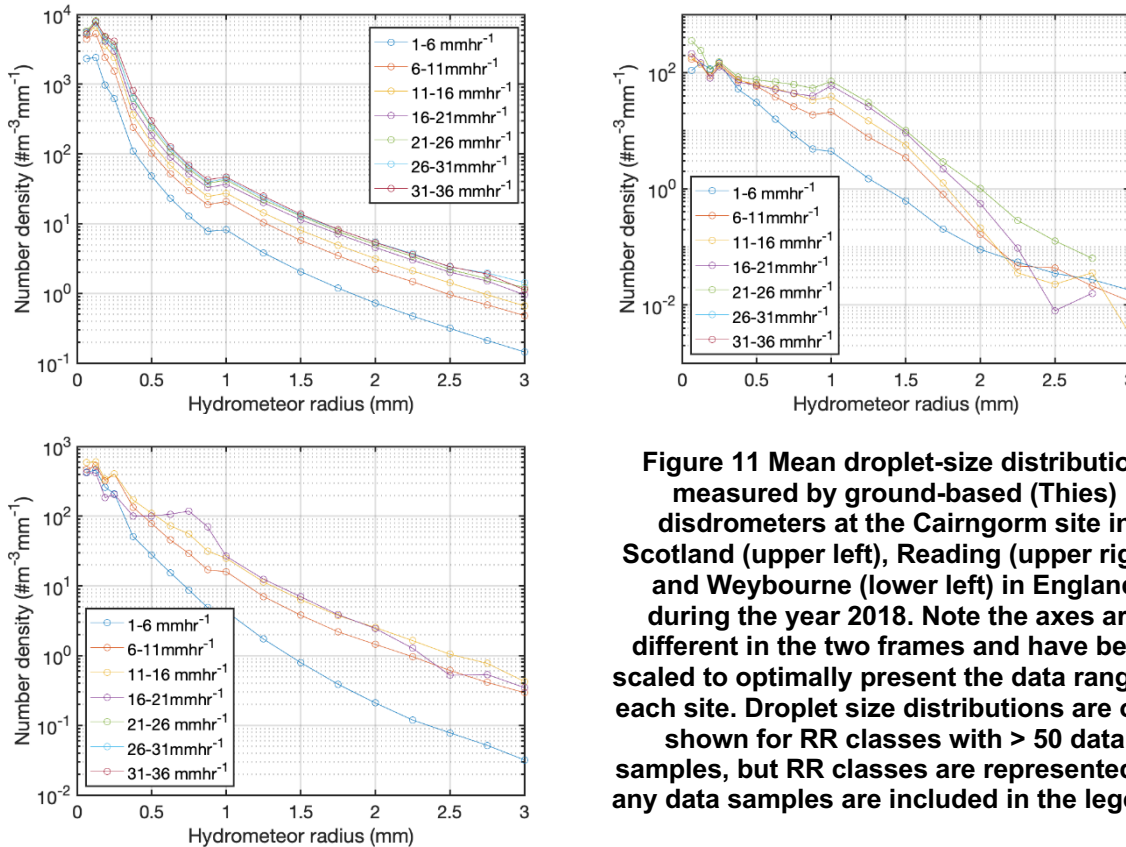


Figure 11 Mean droplet-size distribution measured by ground-based (Thies) disdrometers at the Cairngorm site in Scotland (upper left), Reading (upper right) and Weybourne (lower left) in England during the year 2018. Note the axes are different in the two frames and have been scaled to optimally present the data range at each site. Droplet size distributions are only shown for RR classes with > 50 data samples, but RR classes are represented by any data samples are included in the legend.

4) Figure 12 presents the mean droplet size distributions determined from the precipitation data collected at the offshore National Offshore Anemometry Hub (NOAH) off the Northeast coast of England and the Levenmouth Demonstration Turbine off the East coast of Scotland.

- a. For NOAH: For a rain rate of 6 mmhr^{-1} and 21 mmhr^{-1} , the number concentration of droplets of 1 mm radii is $9.75 \text{ m}^{-3}\text{mm}^{-1}$ and $42.4 \text{ m}^{-3}\text{mm}^{-1}$, respectively. The equivalent concentrations for droplets of 2 mm radii are $< 0.01 \text{ m}^{-3}\text{mm}^{-1}$ and $0.01 \text{ m}^{-3}\text{mm}^{-1}$.
- b. For Levenmouth: For a rain rate of 6 mmhr^{-1} and 21 mmhr^{-1} , the number concentration of droplets of 1 mm radii is $12.5 \text{ m}^{-3}\text{mm}^{-1}$ and $57.5 \text{ m}^{-3}\text{mm}^{-1}$, respectively. The equivalent concentrations for droplets of 2 mm radii are $< 0.01 \text{ m}^{-3}\text{mm}^{-1}$ and $0.03 \text{ m}^{-3}\text{mm}^{-1}$.

Due to the longer measurement period, a greater number of high intensity precipitation events have been recorded at NOAH, whilst a greater number of snow events have been recorded at Levenmouth.

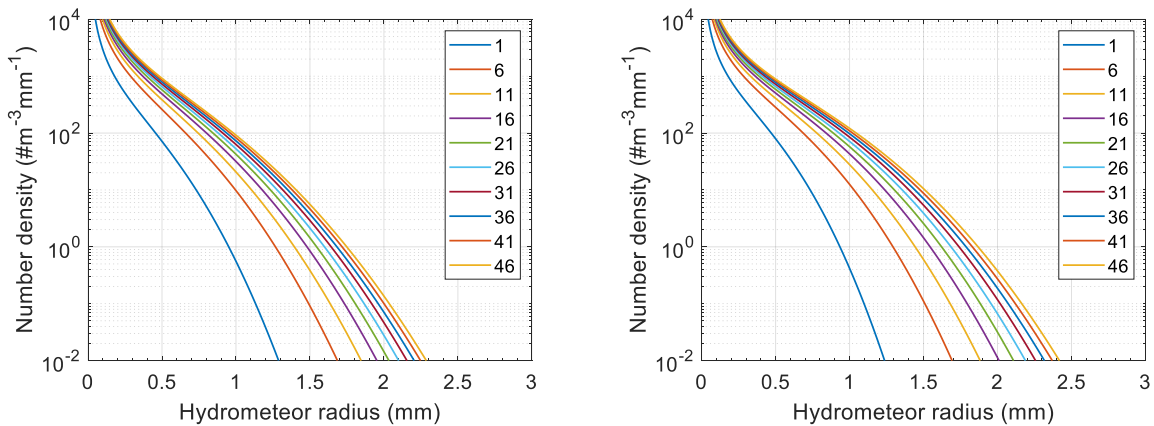


Figure 12 Mean droplet-size distribution across a range of rain rates (mmhr^{-1}) measured by PWS100 Campbell Scientific disdrometers deployed offshore at (left) National Offshore Anemometry Hub off the Northeast coast of England and (right) Levenmouth Demonstration Turbine off the East coast of Scotland from August 2018 and December 2020, respectively, to present. Note periods with higher RR than those displayed have been observed at both sites.

- 5) Figure 13 shows data from ground-based disdrometers at two sites in Denmark:
 - a. The year of data collected at Horns Rev 3 has multiple missing data periods but not a single instance of hail. No class of RR above 6 mmhr^{-1} has more than 50 samples present and no valid data are present for RR above approximately 16 mmhr^{-1} . For a rain rate of $6\text{-}11 \text{ mmhr}^{-1}$ the number concentration of droplets of approx. 1 mm radius is $154 \text{ mm}^{-3} \text{ mm}^{-1}$, for radius of 2 mm the mean number concentration is $1.5 \text{ mm}^{-3} \text{ mm}^{-1}$. Figure 14 shows mean droplet-size distribution at the offshore wind farm Horns Rev 2 (3 year record) and confirms a relatively low frequency of occurrence of $\text{RR} > 10 \text{ mmhr}^{-1}$.
 - b. Data collected during 2019 at DTU indicate a greater frequency of higher RR than at Horns Rev 3, and 15 records indicate the presence of hail. For a rain rate of $6\text{-}11 \text{ mmhr}^{-1}$ the number concentration of droplets of approx. 1 mm radius is $32 \text{ mm}^{-3} \text{ mm}^{-1}$, while for a rain rate of $21\text{-}26 \text{ mmhr}^{-1}$ it is $88 \text{ mm}^{-3} \text{ mm}^{-1}$. Equivalent number concentrations for approximately 2 mm radii droplets are; 1.5 and $3.7 \text{ mm}^{-3} \text{ mm}^{-1}$.

The probability of $RR > 0.2 \text{ mmhr}^{-1}$ is 4.8%. Using a threshold of $RR > 0.2 \text{ mmhr}^{-1}$, the 90th percentile RR is 2.8 mmhr^{-1} and the 99th percentile RR is 10.6 mmhr^{-1} .

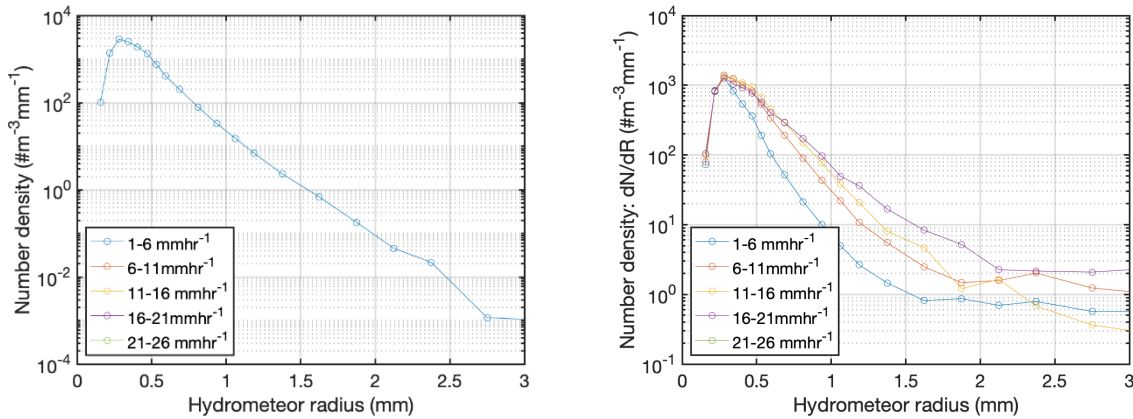


Figure 13 Mean droplet-size distribution measured by a ground-based Parsivel² disdrometers at the Horns Rev 3 wind farm during February 2019 to February 2020 (left) and during 2019 on the DTU campus at Risø (right). Note the axes are different in the two frames and have been scaled to optimally present the data range at each site. There appear to be no valid data at Horns Rev 3 for rainfall rates above approximately 16 mmhr^{-1} .

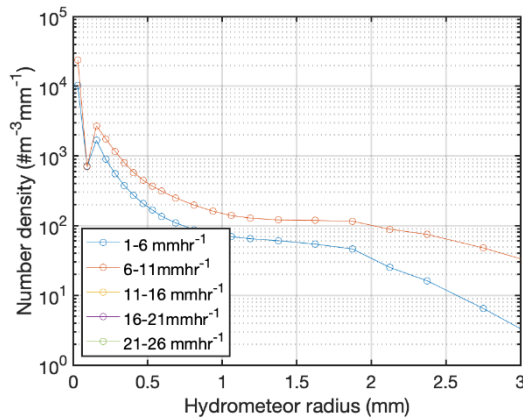


Figure 14 Mean droplet-size distribution measured by a ground-based Parsivel² disdrometer at the Horns Rev 2 wind farm off the west coast of Denmark during December 2018 to October 2021. Note there are very few valid data for rainfall rates above approximately 10 mmhr^{-1} .

The panels in Figures 7-14 and associated descriptive statistics are illustrative of the profound variations in rainfall rate, mean droplet size distributions and hail frequency across the sites from which detailed hydrometeor data are available.

As summarized in Table 6, the mean number concentration for a RR of $21\text{-}26 \text{ mmhr}^{-1}$ at a radius of 1 mm or 2 mm span a factor of nearly five. A key factor in dictating the droplet size distributions is the minimum hydrometeor radius for which data can be obtained. Hence, some of the differences are associated with differences in the instrument metrologies (measurement range) and/or the height for which the data are valid. Nevertheless, the differences in the hydroclimates; probability of precipitation and hail, intensity of precipitation and the size distributions of hydrometeors have profound implications for the number of hydrometeor impacts on the blades of operating wind turbines, the mass associated with those impacts and the materials response.

Table 6 The mean number concentrations of rain droplets expressed in number per cubic meter of air in a size class with a 1 mm diameter (i.e. # m⁻³ mm⁻¹) of a given radius (either 1 mm or 2 mm) derived from the measurements shown in Figure 7-14 and the two theoretical distributions.

	RR = 21 mmhr ⁻¹	
<u>Theoretical distribution</u>	R = 1 mm	R = 2 mm
Marshall-Palmer	104	1.4
Best	37	2.9
	RR = 21-26 mmhr ⁻¹	
<u>Observations</u> (probability of precipitation: RR > 0.2 mmhr ⁻¹ in %)	R = 1 mm	R = 2 mm
&Norway: Bergen (13%)	22	0.2
%Canada: WEICAN (N/A)	N/A	N/A
USA: SGP-Lamont (2.4% impact, 3.2% laser disdrometer)	81	3.9
USA: SGP-Billings (3.0%)	88	2.9
\$UK: Cairngorm (14%)	42	5
\$UK: Reading (6%)	71	1.1
\$UK: Weybourne (6%)	31	3.2
%UK: NOAH (4.2%)	42	0.01
%UK: Levenmouth (6.1%)	58	0.03
Denmark: Horns Rev 2 (5.8%)	N/A	N/A
Denmark: DTU-Risoe (3.8%)	131	1.7

Notes: For qualitative comparison the number concentrations from the Marshall-Palmer and Best droplet distributions are also given for a RR of 21 mmhr⁻¹. The marginal probability of precipitation is given in parentheses after the station location for RR > 0.2 mmhr⁻¹. Sites shown with a \$ denote analyses are based on data from Thies LPM disdrometer. Sites shown with a % denote analyses are based on data from a Campbell Scientific Present Weather sensor. Sites shown with a & denote analyses based on data from a MRR. All other sites use OTT-Parsivel² disdrometers.

4.3 Variability in rainfall rates and droplet size distributions as a function of instrument

Past research has reported substantial difference in rainfall rate and droplet size distributions from different instruments, particularly during heavy rainfall (Tokay et al. 2001; Tokay et al. 2010; Tokay et al. 2013). A study using the three disdrometers types from which data are presented herein; PWS100, Thies LPM and the first-generation OTT-Parsivel (note data from the second generation instrument are presented here) found all underestimated total rainfall compared to the rain gauge with relative biases from 2% to 29% (Johannsen et al. 2020). An additional comparison of OTT Parsivel² (2nd generation) disdrometer and Thies LPM found the Thies instrument gave higher number counts of larger droplets resulting in higher rain rates (Angulo-Martínez et al. 2018). Analysis of data from 318 rainfall events collected using the Parsivel (first-generation) from OTT and the Laser Precipitation Monitor (LPM) from Thies Clima in south-eastern Australia, found the “LPM recorded 1 to 2 orders of magnitude more smaller droplets for drop diameters below 0.6 mm compared to the Parsivel¹, with differences increasing at higher rainfall rates” (Guyot et al. 2019).

While an instrument intercomparison study was beyond the scope of the current work a brief one-week closure experiment using four brand new co-located OTT Parsivel² disdrometers was performed on the Cornell University campus in upstate New York. Rainfall rates and the mean size spectrum are shown in Figure 15 for 2600 1-minute intervals during which precipitation was reported. Slope and intercept values from the scatterplots of 1-minute rainfall rates are based on linear regression fits from the data $D_X = aD_1 + c$, where a is the slope and c is the intercept and D_1 is the disdrometers arbitrarily defined as the reference. As shown, rainfall rates from three of the four disdrometers exhibit very good agreement with best fit lines that have nearly zero intercept and a slope very close to 1. The fourth instrument exhibited higher rainfall rates during almost all 1 minute periods. The mean droplet size spectra illustrate that the third disdrometers (D3) exhibits a higher frequency of droplets with radii in excess of 0.5 mm. A longer data set is being collected to examine causes of this offset in further detail. Work is needed to examine if similar measurement discrepancies between identical instruments from other manufacturers exists.

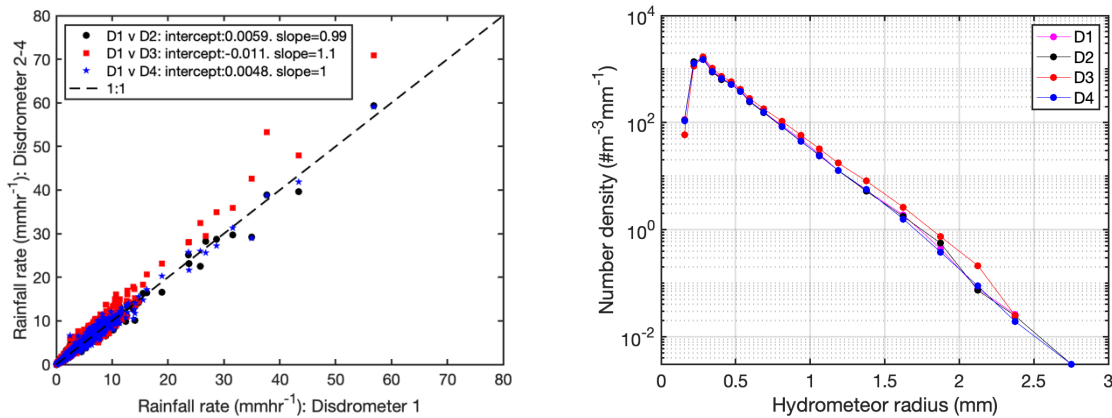


Figure 15 Left: Scatterplots of 1-minute rainfall rates (mmhr^{-1}) from the four disdrometers (D1-D4). Right: Mean droplet size spectrum from those disdrometers. Data collected at Cornell University Ithaca, NY during 21-29 October 2021. 2600 1-minute periods exhibited non-zero RR.

4.4 Variability in droplet size distributions as a function of event and season

The mean droplet size distributions described above in sections 4.2 and 4.3 are useful in illustrating spatial variability in the sizes and numbers of falling hydrometeors but obscure equally important temporal variability. That temporal variability in rainfall rates, size distributions and precipitation kinetic energy is manifest within individual precipitation events, between events and on the seasonal and interannual time scales. The variability in droplet size distributions from minute-to-minute during a precipitation event and between precipitation events is illustrated in Figure 16 which shows the 10th and 90th percentile droplet concentrations by droplet diameter sampled for all periods when the optical disdrometer at Lamont in the US SGP indicates a $\text{RR} > 0.2 \text{ mmhr}^{-1}$. There is also profound seasonality both in precipitation intensity and mean droplet size distributions at this site (Figure 17). At this location, data for 2017-2019 from the optical disdrometer indicates the rate of occurrence of $\text{RR} > 10 \text{ mmhr}^{-1}$ is twice as high in the warm season months (nominally April-September) as during the cold season (nominally January-March and October-December) (Figure 17). Equivalent analyses based on data from the MRR

at Bergen in Norway also show wide variations in droplet size distributions between events (Figure 18) and between rain rates in different seasons (Figure 19). Analysis of six years of data from a Thies disdrometer at a land site in Denmark found that accumulated rainfall kinetic energy peak in summer and autumn. In summer it was due to higher drop concentrations. In autumn it is largely attributable to higher probability of precipitation. There are also important links between droplet size distributions and wind speed (Tilg et al. 2020).

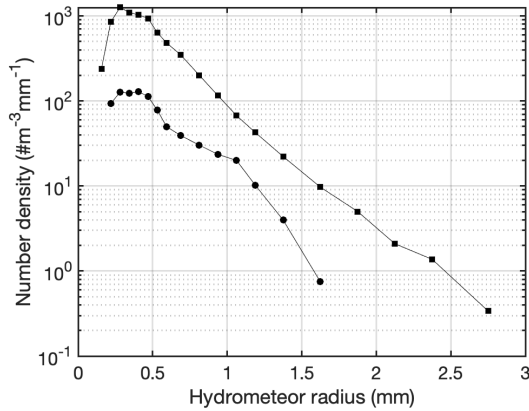


Figure 16 The 10th and 90th percentile values of the droplet number concentration in each size class based on measurements by a ground-based Parsivel² disdrometer at the DoE ARM observatory at Lamont in the U.S. Southern Great Plains during 2019.

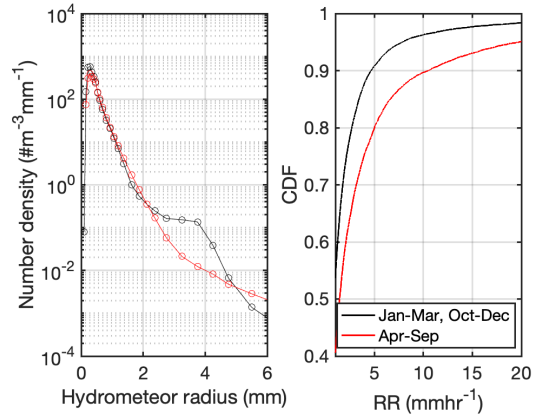


Figure 17 Mean droplet-size distribution measured by a ground-based Parsivel² disdrometer at the DoE ARM observatory at Lamont in the U.S. Southern Great Plains based on data from 2017-2019, inclusive (left). The cumulative probability distribution for RR > 0.2 mmhr⁻¹ based on the same data set. For legibility the x-axis has been truncated to only show RR of 1-20 mmhr⁻¹.

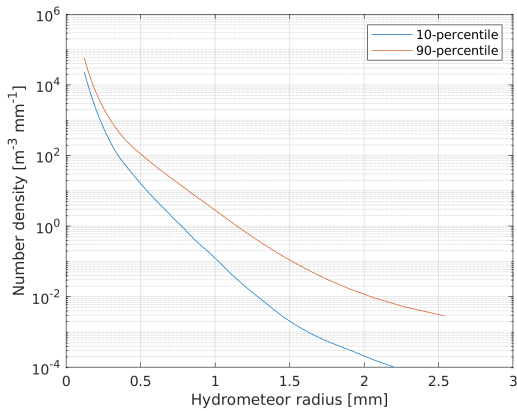


Figure 18 The 10th and 90th percentile values of the droplet number concentration from 100-300 m a.g.l. based on measurements by the MRR at Bergen during 2019.

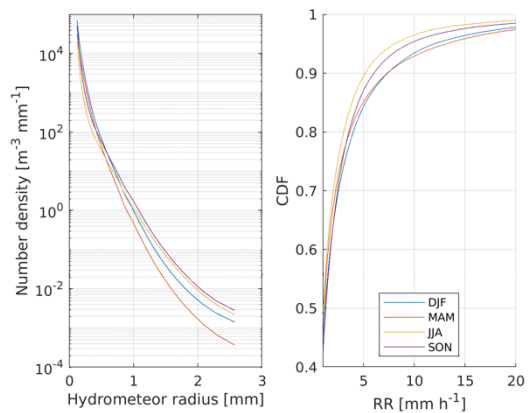


Figure 19 Mean droplet-size distribution in the winter, spring, summer and autumn based on measurements at 100-300 m a.g.l. using the MRR at Bergen during 2017-2019, inclusive (left). The cumulative probability distribution for RR > 0.2 mmhr⁻¹ based on the same data set. For legibility the x-axis has been truncated to only show RR of 1-20 mmhr⁻¹.

Wind speeds also vary across a wide range of time scales and wind turbine rotor tip-speed is a nonlinear function of wind speed. This implies very long data records at a given location may be required to generate joint probability distributions of wind speeds and hydrometeor closing velocities and kinetic energy necessary. These joint probabilities are necessary to make robust assessments of leading edge erosion potential (Letson et al. 2020c). Previous work used a model for incremental damage as a function of the kinetic impact of energy and assumed an IEA 15 MW reference turbine. Their results for the hydroclimate of Denmark indicate that a time series of more than 10 years duration is necessary in order to provide reliable prediction of blade lifetimes (Hasager et al. 2021). Using shorter time series will lead to inaccurate projections of blade lifetime as highly erosive events are sufficiently infrequent to be poorly sampled in short time series.

5 Identification of priority geographic areas for geospatial mapping of wind turbine blade leading edge erosion potential

Data summarized in section 4 indicate the droplet size distributions of hydrometeors, precipitation frequency and intensity and hail frequency vary markedly across the locations considered herein. The implication is that atmospheric conditions associated with leading edge erosion (e.g. frequency of hail and heavy precipitation co-occurring with wind speeds above cut in) will also exhibit large spatial variability across a range of spatial scales. The further inference is there are likely to be large spatial gradients and region-to-region variations in leading edge erosion potential.

Some important findings from recent research in terms of country-to-country and region-to-region variability in wind turbine blade leading edge erosion potential are:

- 1) The state of the art (including data summarized above) suggests there are likely to be pronounced regional differences in terms of the relative importance to total accumulated kinetic energy transfer to the blades of; (i) hail versus rain, (ii) low intensity (low rainfall rates) but sustained precipitation periods versus high intensity but relatively short duration precipitation periods.
- 2) Hail frequency in the USA greatly exceed those in Europe (see above and also (Raupach et al. 2021)). Hail is particularly frequent in regions of the USA with very high wind turbine installed capacity densities. There is emerging evidence that hail is likely the dominant source of leading edge erosion in the USA (Letson et al. 2020b) in contrast to northern Europe where the hydroclimate is dominated by liquid precipitation, hail is very infrequent and thus kinetic energy transfer is likely dominated by rain (Bartolomé and Teuwen 2021; Hasager et al. 2020).
- 3) There are important gradients in hail frequency at the regional and sub-regional scale. Northwestern Texas has high wind turbine installed capacity and high joint probability of hail and/or heavy precipitation and power-producing wind speeds (see also Figure 9). Annual precipitation varies by a factor of 10 across Texas and the prevalence of hail events ranges from hundreds of 5-minute events per year to nearly zero (Letson et al. 2020c).
- 4) The specific instrument (i.e. type of disdrometer) from which DSD are drawn has a profound influence on the resulting DSD (see examples in section 4 and past work (Angulo-Martínez et al. 2018)). Causes of these differences are only partly resolved and the discrepancies in data from different instruments is likely to be a function of the hydroclimate. Instrument closure experiments to resolve these matters and those

arising from difference in instruments from the same manufacturer (see e.g. Figure 15) should be the focus of future efforts within this wind task subject to funding availability. As shown in Figure 20 the locations for which high-quality long-term droplet size distribution data are available for research within this IEA Wind task do not fully overlap with the countries with highest current wind energy installed capacity (notably data from China are not available). Nevertheless, four of the 15 countries with highest wind energy installed capacity are sampled in the data sets compiled for this report (listed in order of ascending IC); Denmark, Canada, UK and USA are available, in addition to Taiwan and Norway which has high wind energy potential along the west coast.

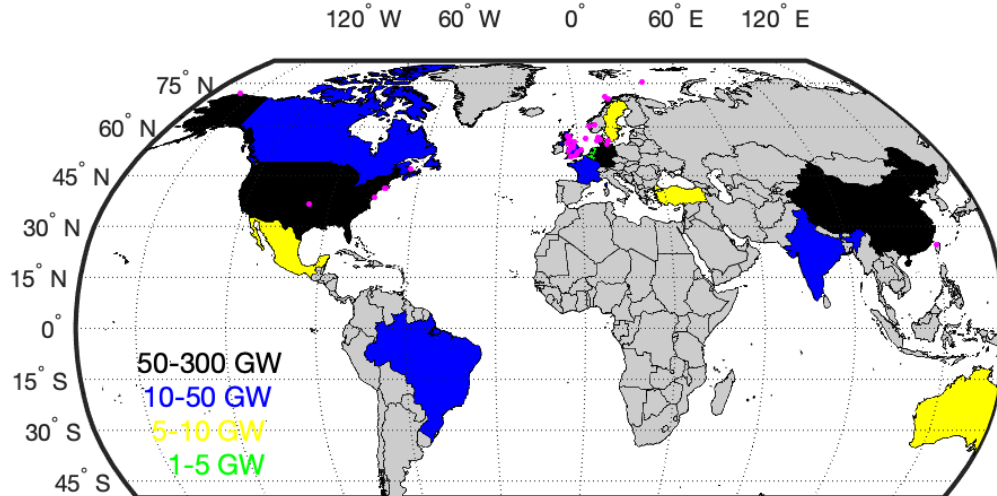


Figure 20 Background: Countries that have either more than 5 GW of wind energy installed capacity (IC) onshore or more than 1.5 GW offshore (as of end of 2020) (data from the GWEC 2020 status report (GWEC 2021)). Countries shaded in black have a total IC of 50-300 GW, in blue 10-50 GW, in yellow 5-10 GW and in green 1-5 GW. The magenta dots indicate the locations for which long-term (> 1 year) of droplet size distributions are available.

Due to the high wind resources and/or wind energy deployments, availability of quality hydro-climatology data and in order to sample across a wide range of hydro-climate and wind regimes, the following sites have been identified for use in future work in IEA Wind Task 46 WorkPackage 2:

- USA: Southern Great Plains U.S. Department of Energy ARM site. This site is selected because of the high quality of data available, high hail presence and proximity to large wind turbine deployments.
- UK: Weybourne. This site is selected because of the high quality of data available, and proximity to large offshore wind turbine deployments.
- Norway: Bergen. This site is selected because it features co-located Micro-rain RADAR and an OTT-Parsivel² disdrometer and is close to areas being considered for floating wind turbine deployments.
- Canada: WEICan. This site is selected due to the proximity to operating wind turbines and a high frequency of freezing rain as a potential co-stressor for leading edge erosion.
- Denmark: Risø campus, DTU. This site is selected due to the presence of a range suite of measurement metrologies.

If possible data collected by a commercial partner at a site in Taiwan and in offshore lease areas along the USA east coast will be included in future analyses subject to data release. Planned future work will focus on co-stressors and building the workflow to develop relative estimates of leading edge erosion potential.

6 Key Conclusions/Recommendations

The following key recommendations may be made based on materials presented above:

- Additional in situ measurements of rain and hail size distributions is urgently needed to help describe and characterize leading edge erosion potential at wind energy deployment locations. The degree to which leading edge erosion is driven primarily by; (i) the few very large diameter droplets associated with low frequency, high intensity events, or (ii) the more moderate droplet diameters and more frequently occurring moderate rainfall rates, is an open question from the industry perspective and, as described herein, it is likely to be location specific. Thus, there is great value in sampling across different hydro-climatic regions.
- The Best droplet size distribution and the Marshall-Palmer size distribution do not fully describe in situ measurements of hydrometeors. Hence, there is a clear need to consider other hydrometeors and to evolve beyond single reliance on the Best droplet size distribution in leading edge erosion testbeds to ensure the conditions to which wind turbine blades will be subject during operation can be properly assessed. Inclusion of solid state hydrometeors in this testing would be advantageous.
- The very limited availability of direct hail measurements at or near operating wind farms represents a key research need and the key importance of investment in such instruments for direct in situ measurements at a range of operating wind farms. At some locations extreme hailstorms could drive the leading edge erosion past incubation, significantly reducing the lifetime compared to cumulative fatigue with many years of moderate rain droplet diameters and rainfall rates. In situ hail and rain measurements will enable research to distinguish the driving factor(s) of damage.
- Enhanced availability of hydrometeor size distributions in the public domain would greatly benefit research into the mechanisms and geographic variability of wind turbine blade leading edge erosion and prove useful for other applications.
- Use of RADAR products may be justified to describe hydroclimatic properties of relevance to wind turbine blade leading edge erosion subject to additional verification and will enable improved description of spatial variability in leading edge erosion potential.
- Hindcast and/or reanalysis products are showing enhanced fidelity. Additional evaluation hindcasts/reanalyses is warranted to establish their fidelity and utility in providing quantitative estimates of supplemental parameters (e.g. UV radiative flux) of importance to wind turbine leading edge erosion.
- Investment in enhanced numerical simulation capabilities for precipitation properties would benefit the wind energy community by enabling robust a priori estimates of leading edge erosion potential prior to wind farm construction.
- Many countries have plans for extensive expansion of wind turbine installed capacity both onshore and offshore (Barthelmie and Pryor 2021). For example, the US has plans to deploy 26-28 GW offshore along the east coast (Pryor et al. 2021). Tip speeds for the larger wind turbines that are likely to be deployed are higher than the current

land-based turbines leading to enhanced closing velocities. Operations and maintenance of offshore wind turbines is considerably more costly than for onshore deployments and is a source of enhanced levelized cost of energy from wind turbines deployed offshore (Ren et al. 2021). Enhanced knowledge of hydroclimates (including the frequency of hail) offshore is urgently needed.

- There would be clear benefit to inter-calibration/instrument closure experiments across a range of different hydroclimates. Further enhancements of instrument durability would also enable collection of long-term data records needed for characterization of leading edge erosion potential in harsh environments (e.g. offshore).

7 References

- Angulo-Martínez, M., S. Beguería, B. Latorre, and M. Fernández-Raga, 2018: Comparison of precipitation measurements by OTT Parsivel 2 and Thies LPM optical disdrometers. *Hydrology and Earth System Sciences*, **22**, 2811-2837.
- Barthelmie, R. J., and S. C. Pryor, 2021: Climate Change Mitigation Potential of Wind Energy. *Climate*, **9**, 136.
- Barthelmie, R. J., P. Doubrawa, H. Wang, G. Giroux, and S. C. Pryor, 2016: Effects of an escarpment on flow parameters of relevance to wind turbines. *Wind Energy*, **19**, 2271-2286.
- Bartolomé, L., and J. Teuwen, 2021: Methodology for the energetic characterisation of rain erosion on wind turbine blades using meteorological data: A case study for The Netherlands. *Wind Energy*, **24**, 686-698.
- Berthet, C., J. Dessens, and J. L. Sánchez, 2011: Regional and yearly variations of hail frequency and intensity in France. *Atmospheric Research*, **100**, 391-400.
- Best, A., 1950: The size distribution of raindrops. *Quarterly Journal of the Royal Meteorological Society*, **76**, 16-36.
- Cheng, L., and M. English, 1983: A relationship between hail stone concentration and size. *Journal of the Atmospheric Sciences*, **40**, 204-213.
- Collier, C. G., 2000: Precipitation estimation and forecasting, World Meteorological Organization, OPERATIONAL HYDROLOGY REPORT No. 46. Available from: .
- Dhiram, K., and Z. Wang, 2016: Evaluation on radar reflectivity-rainfall rate (ZR) relationships for Guyana. *Atmospheric and Climate Sciences*, **6**, 489-499.
- DNVGL, 2020: Evaluation of erosion and delamination for leading edge protection systems of rotor blades, Document #: DNVGL-RP-0573, 44pp. Available from: <https://www.document-center.com/standards/show/DNVGL-RP-0573>.
- Dolan, B., B. Fuchs, S. Rutledge, E. Barnes, and E. Thompson, 2018: Primary modes of global drop size distributions. *Journal of the Atmospheric Sciences*, **75**, 1453-1476.
- Eisenberg, D., S. Laustsen, and J. Stege, 2018: Wind turbine blade coating leading edge rain erosion model: Development and validation. *Wind Energy*, **21**, 942-951.
- Gaertner, E., and Coauthors, 2020: IEA Wind TCP Task 37: Definition of the IEA 15-Megawatt Offshore Reference Wind Turbine. National Renewable Energy Lab.(NREL), Golden, CO (United States). Available for download from: <https://www.osti.gov/biblio/1603478>, 44 pp.
- Guyot, A., J. Pudashine, A. Protat, R. Uijlenhoet, V. Pauwels, A. Seed, and J. P. Walker, 2019: Effect of disdrometer type on rain drop size distribution characterisation: a new

- dataset for south-eastern Australia. *Hydrology and Earth System Sciences*, **23**, 4737-4761.
- GWEC, 2021: *Global wind report 2020*. Global Wind Energy Council, Brussels, Belgium. Available for download from: <https://gwec.net/global-wind-report-2020/>, 78 pp.
- Haakenstad, H., Ø. Breivik, B. R. Furevik, M. Reistad, P. Bohlinger, and O. J. Aarnes, 2021: NORA3: A nonhydrostatic high-resolution hindcast of the North Sea, the Norwegian Sea, and the Barents Sea. *Journal of Applied Meteorology and Climatology*, **60**, 1443-1464.
- Hasager, C., F. Vejen, J. Bech, W. Skrzypiński, A.-M. Tilg, and M. Nielsen, 2020: Assessment of the rain and wind climate with focus on wind turbine blade leading edge erosion rate and expected lifetime in Danish Seas. *Renewable Energy*, **149**, 91-102.
- Hasager, C. B., F. Vejen, W. R. Skrzypiński, and A.-M. Tilg, 2021: Rain Erosion Load and Its Effect on Leading-Edge Lifetime and Potential of Erosion-Safe Mode at Wind Turbines in the North Sea and Baltic Sea. *Energies*, **14**, 1959.
- Hashemi, H., J. Fayne, V. Lakshmi, and G. J. Huffman, 2020: Very high resolution, altitude-corrected, TMPA-based monthly satellite precipitation product over the CONUS. *Scientific data*, **7**, 1-10.
- Heinrich, A., R. Ross, G. Zumwalt, J. Provorse, and V. Padmanabhan, 1991: Aircraft Icing Handbook. Volume 1.
- Herring, R., K. Dyer, P. Howkins, and C. Ward, 2020: Characterisation of the offshore precipitation environment to help combat leading edge erosion of wind turbine blades. *Wind Energy Science*, **5**, 1399-1409.
- Hersbach, H., and Coauthors, 2020: The ERA5 global reanalysis. *Quarterly Journal of the Royal Meteorological Society*, **146**, 1999-2049.
- Herzogh, P. H., and A. R. Jameson, 1992: Observing precipitation through dual-polarization radar measurements. *Bulletin of the American Meteorological Society*, **73**, 1365-1376.
- Johannsen, L. L., and Coauthors, 2020: Comparison of three types of laser optical disdrometers under natural rainfall conditions. *Hydrological Sciences Journal*, **65**, 524-535.
- Jourdier, B., 2020: Evaluation of ERA5, MERRA-2, COSMO-REA6, NEWA and AROME to simulate wind power production over France. *Advances in Science and Research*, **17**, 63-77.
- Kathiravelu, G., T. Lucke, and P. Nichols, 2016: Rain drop measurement techniques: a review. *Water*, **8**, 29.
- Keegan, M. H., D. Nash, and M. Stack, 2013: On erosion issues associated with the leading edge of wind turbine blades. *Journal of Physics D: Applied Physics*, **46**, 383001.
- Klugmann, D., K. Heinsohn, and H.-J. Kirtzel, 1996: A low cost 24 GHz FM-CW Doppler radar rain profiler. *Contributions to atmospheric physics*, **69**, 247-253.
- Kochendorfer, J., and Coauthors, 2020: Undercatch adjustments for tipping-bucket gauge measurements of solid precipitation. *Journal of Hydrometeorology*, **21**, 1193-1205.
- Krajewski, W. F., and J. A. Smith, 1991: On the estimation of climatological Z–R relationships. *Journal of Applied Meteorology and Climatology*, **30**, 1436-1445.
- Labriola, J., N. Snook, Y. Jung, and M. Xue, 2019: Explicit ensemble prediction of hail in 19 May 2013 Oklahoma City thunderstorms and analysis of hail growth processes with several multimoment microphysics schemes. *Monthly Weather Review*, **147**, 1193-1213.

- Letson, F., T. J. Shepherd, R. J. Barthelmie, and S. C. Pryor, 2020a: WRF modelling of deep convection and hail for wind power applications. *Journal of Applied Meteorology and Climatology*, **59**, 1717-1733.
- Letson, F. W., R. J. Barthelmie, and S. C. Pryor, 2020b: RADAR-derived precipitation climatology for wind turbine blade leading edge erosion. *Wind Energy Science*, **5**, 331-347.
- Letson, F. W., R. J. Barthelmie, and S. C. Pryor, 2020c: Sub-regional variability in wind turbine blade leading-edge erosion potential. *Journal of Physics Conference Series. Science of Making Torque from Wind.*, **1618**, 032046 doi:032010.031088/031742-036596/031618/032043/032046.
- Li, S., R. J. Barthelmie, G. P. Bewley, and S. C. Pryor, 2020: Quantifying hydrometeor droplet impact probabilities for wind turbine blade leading edge erosion analyses. *Journal of Physics: Conference Series*, **1452**, 012053, doi: 012010.011088/011742-016596/011452/012051/012053/.
- Löffler-Mang, M., M. Kunz, and W. Schmid, 1999: On the performance of a low-cost K-band Doppler radar for quantitative rain measurements. *Journal of Atmospheric and Oceanic Technology*, **16**, 379-387.
- Marshall, J. S., and W. M. K. Palmer, 1948: The distribution of raindrops with size. *Journal of meteorology*, **5**, 165-166.
- Pickering, B. S., R. R. Neely III, and D. Harrison, 2019: The Disdrometer Verification Network (DiVeN): A UK network of laser precipitation instruments. *Atmospheric Measurement Techniques*, **12**, 5845-5861.
- Počakal, D., Ž. Večenaj, and J. Štalec, 2009: Hail characteristics of different regions in continental part of Croatia based on influence of orography. *Atmospheric Research*, **93**, 516-525.
- Prieto, R., and T. Karlsson, 2021: A model to estimate the effect of variables causing erosion in wind turbine blades. *Wind Energy*, **24**, 1031-1044.
- Pryor, S. C., F. W. Letson, and R. J. Barthelmie, 2020: Variability in wind energy generation across the contiguous USA. *Journal of Applied Meteorology and Climatology* **59**, 2021-2039.
- Pryor, S. C., R. J. Barthelmie, and T. J. Shepherd, 2021: Wind power production from very large offshore wind farms. *Joule*, **5**, 2663-2686.
- Raupach, T. H., and A. Berne, 2015: Correction of raindrop size distributions measured by Parsivel disdrometers, using a two-dimensional video disdrometer as a reference. *Atmospheric Measurement Techniques*, **8**, 343-365.
- Raupach, T. H., and Coauthors, 2021: The effects of climate change on hailstorms. *Nature Reviews Earth & Environment*, **2**, 213-226.
- Reges, H. W., N. Doesken, J. Turner, N. Newman, A. Bergantino, and Z. Schwalbe, 2016: CoCoRaHS: The evolution and accomplishments of a volunteer rain gauge network. *Bulletin of the American Meteorological Society*, **97**, 1831-1846.
- Ren, Z., A. S. Verma, Y. Li, J. J. Teuwen, and Z. Jiang, 2021: Offshore wind turbine operations and maintenance: A state-of-the-art review. *Renewable and Sustainable Energy Reviews*, **144**, 110886.
- Renfrew, I. A., and Coauthors, 2019: The Iceland Greenland Seas Project. *Bulletin of the American Meteorological Society*, **100**, 1795-1817.

- Sarkar, T., S. Das, and A. Maitra, 2015: Assessment of different raindrop size measuring techniques: Inter-comparison of Doppler radar, impact and optical disdrometer. *Atmospheric Research*, **160**, 15-27.
- Skofronick-Jackson, G., D. Kirschbaum, W. Petersen, G. Huffman, C. Kidd, E. Stocker, and R. Kakar, 2018: The Global Precipitation Measurement (GPM) mission's scientific achievements and societal contributions: reviewing four years of advanced rain and snow observations. *Quarterly Journal of the Royal Meteorological Society*, **144**, 27-48.
- Straka, J. M., D. S. Zrnić, and A. V. Ryzhkov, 2000: Bulk hydrometeor classification and quantification using polarimetric radar data: Synthesis of relations. *Journal of Applied Meteorology*, **39**, 1341-1372.
- Stull, R. B., 2017: *Practical Meteorology: An Algebra-based Survey of Atmospheric Science*. Univ. of British Columbia, ISBN: 978-0-88865-283-6, 940 pp.
- Tapiador, F. J., and Coauthors, 2017: On the optimal measuring area for pointwise rainfall estimation: A dedicated experiment with 14 laser disdrometers. *Journal of Hydrometeorology*, **18**, 753-760.
- Tarek, M., F. P. Brissette, and R. Arsenault, 2020: Evaluation of the ERA5 reanalysis as a potential reference dataset for hydrological modelling over North America. *Hydrology and Earth System Sciences*, **24**, 2527-2544.
- Thurai, M., P. Gatlin, V. Bringi, W. Petersen, P. Kennedy, B. Notaroš, and L. Carey, 2017: Toward completing the raindrop size spectrum: Case studies involving 2D-video disdrometer, droplet spectrometer, and polarimetric radar measurements. *Journal of Applied Meteorology and Climatology*, **56**, 877-896.
- Tilg, A.-M., F. Vejen, C. B. Hasager, and M. Nielsen, 2020: Rainfall Kinetic Energy in Denmark: Relationship with Drop Size, Wind Speed, and Rain Rate. *Journal of Hydrometeorology*, **21**, 1621-1637.
- Tilg, A.-M., M. Hagen, F. Vejen, and C. B. Hasager, 2021: Variation of leading-edge-erosion relevant precipitation parameters with location and weather type. *Meteorol. Z.*, **30**, 251-269.
- Tokay, A., A. Kruger, and W. F. Krajewski, 2001: Comparison of drop size distribution measurements by impact and optical disdrometers. *Journal of Applied Meteorology and Climatology*, **40**, 2083-2097.
- Tokay, A., P. G. Bashor, and V. L. McDowell, 2010: Comparison of rain gauge measurements in the mid-Atlantic region. *Journal of Hydrometeorology*, **11**, 553-565.
- Tokay, A., D. B. Wolff, and W. A. Petersen, 2014: Evaluation of the new version of the laser-optical disdrometer, OTT Parsivel2. *Journal of Atmospheric and Oceanic Technology*, **31**, 1276-1288.
- Tokay, A., W. A. Petersen, P. Gatlin, and M. Wingo, 2013: Comparison of raindrop size distribution measurements by collocated disdrometers. *Journal of Atmospheric and Oceanic Technology*, **30**, 1672-1690.
- Tokay, A., P. Hartmann, A. Battaglia, K. S. Gage, W. L. Clark, and C. R. Williams, 2009: A field study of reflectivity and Z-R relations using vertically pointing radars and disdrometers. *Journal of Atmospheric and Oceanic Technology*, **26**, 1120-1134.
- Ulbrich, C. W., and D. Atlas, 1998: Rainfall microphysics and radar properties: Analysis methods for drop size spectra. *Journal of Applied Meteorology*, **37**, 912-923.

Wijayarathne, D., and P. Coulibaly, 2021: Application of weather Radar for operational hydrology in Canada—a review. *Canadian Water Resources Journal/Revue canadienne des ressources hydriques*, **46**, 17-37.

Witt, A., M. D. Eilts, G. J. Stumpf, J. Johnson, E. D. W. Mitchell, and K. W. Thomas, 1998: An enhanced hail detection algorithm for the WSR-88D. *Weather and Forecasting*, **13**, 286-303.

8 Appendix A: Vocabularies/definitions

The following provides a brief summary of key list of terms from a range of vocabularies.

8.1 Relevant definitions from the World Meteorological Organization

According to the World Meteorological Organization (<https://cloudatlas.wmo.int/>) the following classes of falling precipitation can be defined:

- Rain: Precipitation of drops of water that falls from a cloud.
- Supercooled rain: Rain where the temperature of drops is below 0 °C.
- Drizzle: Fairly uniform precipitation of very fine drops of water very close to one another that falls from a cloud.
- Supercooled drizzle: Drizzle where the temperature of drops is below 0 °C.
- Snow: Precipitation of ice crystals, singly or stuck together, that falls from a cloud.
- Snow grains: Precipitation of very small opaque white particles of ice that falls from a cloud. These particles are fairly flat or elongated. Their diameter is generally less than 1 mm.
- Snow pellets (also known as graupel): Precipitation of white and opaque ice particles that falls from a cloud. These particles are generally conical or rounded, and their diameter may be as large as 5 mm.
- Diamond dust: Precipitation that falls from a clear sky in very small ice crystals, often so tiny that they appear to be suspended in the air.
- Hail: Precipitation of particles of ice (hail stones). These can be either transparent, or partly or completely opaque. They are usually spheroidal, conical or irregular in form, and generally 5–50 mm in diameter. The particles may fall from a cloud either separately or agglomerated in irregular lumps.
- Small hail: Precipitation of translucent ice particles that falls from a cloud. These particles are almost always spherical and sometimes have conical tips. Their diameter may approach and even exceed 5 mm.
- Ice pellets: Precipitation of transparent ice particles that falls from a cloud. These particles are usually spheroidal or irregular, and rarely conical. Their diameter is less than 5 mm.

8.2 Relevant definitions from the International Electrotechnical Commission

Per definitions by the International Electrotechnical Commission are given in electropedia.org:

- Precipitation intensity and rain rate are used interchangeably. They are generally expressed in mm per hour and represent the height of water reaching the ground in a time interval divided by the duration of the time interval.

8.3 Relevant definitions from the ontology hosted at DTU Wind Energy

The following vocabulary definitions are available at; <http://data.windenergy.dtu.dk/ontologies/view/en/> .

From ASPECT: wind energy vAriableS ParametErs and ConsTants

- Rainfall_rate: Amount of rain that would fall over a given interval of time if the rainfall rate were constant over that time period (preferred unit mmhr⁻¹)

- Rainfall_kinetic_energy: Energy provided by rain per area and time interval (preferred unit: $\text{Jm}^{-2}\text{hr}^{-1}$)

8.4 World Meteorological Organization (WMO) synoptic present weather codes (Table 4680):

Codes employed the Thies laser disdrometers are shown in bold

40 PRECIPITATION

41 Precipitation, slight or moderate

42 Precipitation, heavy

43 Liquid precipitation, slight or moderate

44 Liquid precipitation, heavy

45 Solid precipitation, slight or moderate

46 Solid precipitation, heavy

47 Freezing precipitation, slight or moderate

48 Freezing precipitation, heavy

49 Reserved

50 DRIZZLE

51 Drizzle, not freezing, slight

52 Drizzle, not freezing, moderate

53 Drizzle, not freezing, heavy

54 Drizzle, freezing, slight

55 Drizzle, freezing, moderate

56 Drizzle, freezing, heavy

57 Drizzle and rain, slight

58 Drizzle and rain, moderate or heavy

59 Reserved

60 RAIN

61 Rain, not freezing, slight

62 Rain, not freezing, moderate

63 Rain, not freezing, heavy

64 Rain, freezing, slight

65 Rain, freezing, moderate

66 Rain, freezing, heavy

67 Rain (or drizzle) and snow, slight

68 Rain (or drizzle) and snow, moderate or heavy

69 Reserved

70 SNOW

71 Snow, slight

72 Snow, moderate

73 Snow, heavy

74 Ice pellets, slight

75 Ice pellets, moderate

76 Ice pellets, heavy

77 Snow grains

78 Ice crystals

79 Reserved

80 SHOWER(S) or INTERMITTENT PRECIPITATION

81 Rain shower(s) or intermittent rain, slight

82 Rain shower(s) or intermittent rain, moderate

83 Rain shower(s) or intermittent rain, heavy

84 Rain shower(s) or intermittent rain, violent

85 Snow shower(s) or intermittent snow, slight

86 Snow shower(s) or intermittent snow, moderate

87 Snow shower(s) or intermittent snow, heavy

88 Reserved

89 Hail

90 THUNDERSTORM

91 Thunderstorm, slight or moderate, with no precipitation

92 Thunderstorm, slight or moderate, with rain showers and/or snow showers

93 Thunderstorm, slight or moderate, with hail

94 Thunderstorm, heavy, with no precipitation

95 Thunderstorm, heavy, with rain showers and/or snow showers

96 Thunderstorm, heavy, with hail

97-98 Reserved

99 Tornado

9 Appendix B: METADATA

Accompanying this report is an excel spreadsheet of metadata for sites from which hydrometeor size distribution data and/or hail occurrence are available. That file is entitled: IEA46_WP2_METADATA_Deliverable1_5November2021.xlsx. The doi for this metadata dataset is 10.5281/zenodo.5648211.